Computers and Geotechnics 148 (2022) 104791

Contents lists available at ScienceDirect

Computers and Geotechnics

journal homepage: www.elsevier.com/locate/compgeo

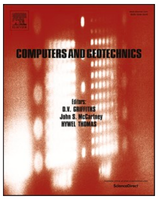

Numerical modeling of seepage and deformation of unsaturated slope subjected to post-earthquake rainfall

Jiawei Xu *, Kyohei Ueda, Ryosuke Uzuoka

Disaster Prevention Research Institute, Kyoto University, Gokasho, Uji, Kyoto 611-0011 Japan

ARTICLE INFO

Keywords:
Numerical modeling
Hydro-mechanical response
Unsaturated slope
Post-earthquake rainfall
Finite element
Centrifuge experiment

ABSTRACT

Slope is susceptible to rainfall-induced failure after being damaged by earthquake. In this study, the seepage and deformation of unsaturated slope during post-earthquake rainfall were investigated using the finite element method. Shaking-induced plastic modulus reduction dependent on deviatoric strain and shaking-induced permeability change dependent on volumetric strain were considered in the modeling of slope response to the following rainfall; the damage concept was adopted to describe shaking-induced cracks and assess the impact of surface cracks on permeability enhancement and strength reduction. Then, numerical modeling of the hydro-mechanical response of slope to rainfall was performed with the updated model. Analysis showed that earthquake significantly affected the slip surface of slope subjected to the following rainfall since soil with reduced shear modulus further deformed, causing a more severe landslide, whereas the influence of earthquake-induced permeability reduction was not great; earthquake-induced damage should be incorporated in the analysis of slope response to rainfall since it altered landslide characteristics. Analysis was generally consistent with centrifuge experiments based on the discussions of pore water pressure, stress path, slope deformation, and soil displacement in simulations and experiments. The coupled hydro-mechanical analysis with the proposed modeling methods could evaluate the response of unsaturated slope to post-earthquake rainfall.

1. Introduction

Rainfall-induced landslide is among the most common disasters in the world (Petley, 2012; Froude and Petley, 2018) and has become the subject of intensive research in the past decades. A considerable amount of literature has been published on the topic. Typical studies consist of the evaluation of the slope failure mechanisms under different conditions (Moriwaki et al., 2004; Take et al., 2004; Wang and Sassa, 2001; Wang et al., 2021), modeling of the effect of vegetation on slope stability during rainfall (Ng et al., 2016; Ni et al., 2018; Switala and Wu, 2018), assessment of the performance of reinforced slopes subjected to rainfall (Cheuk et al., 2005; Yang et al., 2018; Bhattacherjee and Viswanadham, 2019), and numerical simulation of the rainfall-induced landslides in the field (Chen et al., 2021; Tang et al., 2019; Liu et al., 2020). The corresponding findings have considerably improved people's understanding of slope behavior during rainfall and greatly contributed to landslide prediction and prevention.

However, another type of rainfall-induced landslide, originating from the slope with earthquake-induced cracks, has become a growing concern in the field of geological disaster prevention and mitigation recently. The common occurrence of this landslide is that once the earthquake causes tensile cracks on the slope surface, water infiltration during the subsequent rainfall causes the complete failure of the slope. Preliminary studies of this kind of geo-hazard have been carried out by researchers based on aerial images and field investigation. Tang et al. (2011) reported the landslides caused by the 2008 Wenchuan earthquake and the following heavy rainfall in an area near the epicenter, and investigated the correlation between landslide occurrence and post-earthquake rainfall based on the aerial images. Most of the rainfall-induced landslides were found to have occurred due to the co-seismic weakening and the presence of numerous extension cracks generated by the earthquake. Field observations also indicated that slopes that experienced earthquakes required special attention since they were vulnerable to subsequent rainfall. Thus, the restoration in the earthquake-struck areas should consider this impact. Usui et al. (2013) investigated the reason for a massive slope failure caused by rainfall. The extensive distribution of significant cracks along the edge of a terrace cliff was detected right after the 2011 Great East Japan

---

* Corresponding author.
E-mail addresses: xu.jiawei.4n@kyoto-u.ac.jp (J. Xu), ueda.kyohei.2v@kyoto-u.ac.jp (K. Ueda), uzuoka.ryosuke.6z@kyoto-u.ac.jp (R. Uzuoka).

https://doi.org/10.1016/j.compgeo.2022.104791
Received 19 December 2021; Received in revised form 8 March 2022; Accepted 23 April 2022

Earthquake, but the complete slope failure was caused by the intense rainfall six months later. The field survey showed that the increase in pore water pressure because of the rainfall infiltration along the fractured zone triggered the massive landslide that destroyed residence houses at the slope bottom. Lin et al. (2004) and Khattak et al. (2010) also noticed that extensive fissures and ground cracks presented possibilities for future landslides during the rainy season in areas affected by the 1999 Chi-Chi earthquake and the 2005 Kashmir earthquake. Although these studies have implied the importance of earthquake-induced cracks to the slope failure during rainfall, there has been little quantitative analysis of this phenomenon and the comprehensive investigation is inadequate.

Indeed, Xu et al. (2022) found the failure of slopes with shaking-induced cracks was rather different from the slope failure caused by only rainfall and the rainfall intensity played a significant role in the deformation pattern. However, the investigation was conducted by means of physical modeling, and the numerical modeling of the slope failure was still lacking. Since numerical simulation is capable of carrying out parametric studies and examining various cases in a cost-effective way, it is among the favored approaches in the studies of rainfall-induced landslides and also a mainstream methodology in disaster prediction and prevention. Thus, the application of numerical analysis of slope behavior during post-earthquake rainfall can not only enhance the comprehensive understanding of the slope failure mechanism but also contribute to the current practice of landslide prediction and prevention.

The unsaturated soil is a three-phase material consisting of solid, water, and air, so the study of unsaturated soil requires the three-phase analysis. Typical studies included simulations of element tests on unsaturated soil (Khalili et al., 2008; Noda and Yoshikawa, 2015; Ghorbani et al., 2021), investigations of seepage or rainfall induced failure of embankment or slope (Ehlers and Ammann, 2004; Mori et al., 2011; Xiong et al., 2014; Yerro et al., 2015; Zhang et al., 2014; Chen et al., 2021), the seismic behavior of dam or embankment (Ravichandran and Muraleetharan, 2009; Khoei and Mohammadnejad, 2011; Matsumaru and Uzuoka, 2016; Yoshikawa et al., 2016), and dynamic response of unsaturated soil with different conditions (Uzuoka and Borja, 2012; Ghorbani et al., 2020). Especially in the area related to this study, i.e., seepage or rainfall induced failure of embankment or slope, numerical modeling of the rainfall-induced landslide in the field and the corresponding failure mechanism investigation have been conducted by various researchers (Laloui et al., 2016; Yang et al., 2017; Tang et al., 2019; Sitarenios et al., 2021), as well as the study of the rainfall-induced failure of slope with desiccation cracks (Gao et al., 2021); the simulation of the post-failure landslide was also seen in recent studies using the material point method (Liu et al., 2020; Cuomo et al., 2021) or coupled Eulerian–Lagrangian method (Chen et al., 2021). Besides, Hu et al. (2011) examined the impact of gas flow on the coupled solid–water–air process in the unsaturated slope under rainfall and demonstrated the delaying effect of gas flow on the wetting process during the rainfall infiltration into slope. Later on, Hu et al. (2016) further investigated the effects of bonding stress, deformation dependence of water retention behavior, and gas flow on the solid–water–air couplings in unsaturated soil, concluding that the slope deformation would be underestimated when the bonding stress was neglected and further underestimated when the water retention curve and hydraulic conductivity permeability were independent of soil deformation, but it would be overestimated when the gas flow was ignored. These studies usually adopted the theory of porous media (Biot, 1941, 1962) and various constitutive models to incorporate the interaction between solid and fluid phases, and the corresponding theoretical frameworks and applications have widely promoted the understanding of different unsaturated soil problems.

Since the rainfall-induced slope instability or failure involves the hydraulic and mechanical responses of unsaturated soil, uncoupled and coupled hydro-mechanical methods are two methods used in current analyses. In uncoupled hydro-mechanical analysis, seepage analysis is first conducted to generate the pore water pressures in the slope, where the hydraulic response is studied considering hydraulic properties, rainfall features, etc. Then the generated pore water pressures are used for the analysis of the mechanical response of slope, such as the stability analysis based on the limit equilibrium method (Cai and Ugai, 2004; Qi and Vanapalli, 2015). However, the coupled hydro-mechanical analysis enables the interaction between these two responses in the process of rainfall infiltration, thus demonstrating a good performance in reproducing slope behavior during rainfall (Borja and White, 2010; Qi and Vanapalli, 2015; Oh and Lu, 2015; Yang et al., 2017) and becoming a commonly employed method for solving the related issues (Laloui et al., 2016; Tang et al., 2019; Liu et al., 2020; Chen et al., 2021; Sitarenios et al., 2021). In addition, since the finite element method (FEM) has become a widely adopted method in modeling slope failure caused by rainfall (Borja and White, 2010; Laloui et al., 2016; Tang et al., 2019; Sitarenios et al., 2021), the findings obtained using this method could be readily referred to by other researchers and thus promote the understanding of the relevant issue. Based on these reasons, the hydro-mechanically coupled analysis was adopted to investigate the slope behavior during post-earthquake rainfall based on FEM.

Despite the previous studies related to the numerical modeling of rainfall-induced slope failure, the modeling of rainfall-caused slope failure considering the influence of previous earthquakes was quite rare, which was attributed to persisting uncertainties that could affect the simulation outcome and difficulty in accurately assessing them in the constitutive model. These uncertain factors included the plastic modulus degradation, deformation-dependent soil property change, and the effect of shaking-induced cracks on soil strength and permeability. Another difficulty was the modeling of crack generation, which required extensive studies of the constitutive behavior of cracks (Wang et al., 2018). Alternately, some other studies have ignored the generation of cracks and assumed the crack location in the slope (Wang et al., 2011; Utili, 2013; Wang et al., 2019; Zeng et al., 2020) in a way to assess the effect of crack on the slope stability under rainfall using FEM (Wang et al., 2011; Zeng et al., 2020; Zhang et al., 2020). They provided some insight into the behavior of crack-containing slopes during rainfall, which helped the prevention of landslides and the method could be readily employed in the current practice. Nevertheless, the acquired results were rather limited since the focuses were usually on the stability analysis using the limit equilibrium method (Wang et al., 2011; Zeng et al., 2020; Zhang et al., 2020; Zhang et al., 2021). The cracks were artificially designated to the slope models without any prior analysis of the crack location or additional physical experiments and the results tended to vary due to different parametric settings, so this approach had its own drawbacks in the analysis of the effect of earthquake-induced cracks on slope deformation during rainfall. Furthermore, many of these studies involved the desiccation cracks, which had different features compared to earthquake-induced cracks. According to the field survey conducted by Li and Zhang (2010), the desiccation cracks are inter-connected polygons such as quadrilateral, pentagon, and hexagon, forming a random crack network. The location of cracks follows a uniform distribution whereas the length and aperture follow a lognormal distribution. Temperature (Morris et al., 1992; Levatti et al., 2019), relative humidity (Levatti et al., 2019), and soil properties (Morris et al., 1992; Peron et al., 2009; Gao et al., 2021) are common factors affecting the cracks in drying soil. As drying proceeds and the matric suction increases, dominant cracks tend to grow in plain both length and depth. Their depth is ultimately constrained by the increasing stress due to the self-weight of the soil and their length is limited by intersection with other cracks (Morris et al., 1992). The depth of desiccation cracks in the field can be estimated based on the analytical models (Morris et al., 1992; Konrad and Ayad, 1997; Lu and Likos, 2004). However, the earthquake-induced cracks are different from desiccation cracks. The characteristics of earthquake-induced tensile cracks in slopes usually depend on factors such the earthquake intensity and wave form (Oka et al., 2012), topographic amplification (Stahl et al., 2014), and geological condition (Liu et al., 2020). Previously, tensile cracks were found on the slope crest and near the shoulder after the 1968 Tokachi-oki Earthquake (Kobayashi, 1971), the 2008 Wenchuan Earthquake (Huang et al., 2012), and the 2011 Great East Japan Earthquake (Usui et al., 2013). In the reconnaissance after the Great East Japan Earthquake (Oka et al., 2012), longitudinal cracks near/on the crest of embankment due to the lateral expansion of the slope near the toe and the settlement of crest were found in several embankments.

This study aimed to provide a simplified analysis method for addressing the abovementioned problems that could be integrated into the current modeling framework and assessment practice. The simulations of slopes subjected to different external conditions (i.e., rainfall, earthquake, and post-earthquake rainfall) were performed in this study. Pore water pressure, stress path, slope deformation, and soil displacement were the main subjects of thorough examination. The performance of the proposed method was evaluated by comparison of the analyses with the centrifuge experimental results.

2. Coupled hydro-mechanical method

For the soil slope that is partially saturated, the material is composed of three phases, namely, solid skeleton, pore water, and pore air. Thus, the three-phase hydro-mechanically coupled analysis (Mori et al., 2011; Uzuoka and Borja, 2012; Matsumaru and Uzuoka, 2016) were carried out in this study to examine the response of unsaturated slopes to earthquake and rainfall.

2.1. Governing equations

The unsaturated porous media consist of three different phases: solid, water, and air. The solid phase constitutes the soil skeleton while the water and air phases fill the voids. The governing equations of the unsaturated porous media are derived based on the porous media theory (de Boer, 2000; Schrefler, 2002), with assumptions of incompressible soil particle, no temperature change, no mass exchange between the solid particle and fluids, neglected advection terms of pore fluids, and neglected relative accelerations of pore fluids with respect to solid. The mass and momentum balance equations of the solid–water–air mixture (Uzuoka and Borja, 2012) governing the balance laws are briefly presented below.

The density of each phase is defined based on the concept of volume fraction (Lewis and Schrefler, 1998), with expressions of

$$\rho^{\mathrm{s}} = (1-n)\rho^{\mathrm{s}0},\ \rho^{\mathrm{w}} = ns^{\mathrm{w}}\rho^{\mathrm{w}0},\ \text{and}\ \rho^{\mathrm{a}} = ns^{\mathrm{a}}\rho^{\mathrm{a}0} \tag{1}$$

where $\rho^{\mathrm{s}0}$, $\rho^{\mathrm{w}0}$, and $\rho^{\mathrm{a}0}$ are the densities of solid, water, and air; n is the porosity; s^{w} and s^{a} are the degrees of water and air saturation, and $s^{\mathrm{w}} + s^{\mathrm{a}} = 1$.

The mass balance equation of each phase is written as

$$\frac{\partial\rho^{\mathrm{s}}}{\partial t}+\mathrm{div}(\rho^{\mathrm{s}}\boldsymbol{v}^{\mathrm{s}})=0;\ \frac{\partial\rho^{\mathrm{w}}}{\partial t}+\mathrm{div}(\rho^{\mathrm{w}}\boldsymbol{v}^{\mathrm{w}})=0;\ \frac{\partial\rho^{\mathrm{a}}}{\partial t}+\mathrm{div}(\rho^{\mathrm{a}}\boldsymbol{v}^{\mathrm{a}})=0 \tag{2}$$

where $\boldsymbol{v}^{\mathrm{s}}$, $\boldsymbol{v}^{\mathrm{w}}$, and $\boldsymbol{v}^{\mathrm{a}}$ stand for the velocities of solid phase, water phase, and air phase.

The momentum balance equation of the mixture is written as

$$\rho^{\mathrm{m}}\boldsymbol{a}^{\mathrm{s}} = \mathrm{div}\,\boldsymbol{\sigma} + \rho^{\mathrm{m}}\boldsymbol{b} \tag{3}$$

where ρ^{m} is the density of the mixture equivalent to $\rho^{\mathrm{s}} + \rho^{\mathrm{w}} + \rho^{\mathrm{a}}$; $\boldsymbol{a}^{\mathrm{s}}$, $\boldsymbol{a}^{\mathrm{w}}$, and $\boldsymbol{a}^{\mathrm{a}}$ are the accelerations of solid phase, water phase, and air phase; $\boldsymbol{\sigma}$ is the total stress tensor of the mixture; $\boldsymbol{b}$ is the body force vector.

The momentum balance equations of water and air phases are

$$ns^{\mathrm{w}}\boldsymbol{v}^{\mathrm{ws}} = \frac{k^{\mathrm{w}}}{\rho^{\mathrm{w}0}g}\left\{-\mathrm{grad}\,p^{\mathrm{w}} + \rho^{\mathrm{w}0}(\boldsymbol{b}-\boldsymbol{a}^{\mathrm{s}})\right\} \tag{4}$$

$$ns^{a}\boldsymbol{v}^{\mathrm{as}} = \frac{k^{\mathrm{a}}}{\rho^{\mathrm{a}0}g}\left\{-\mathrm{grad}\,p^{\mathrm{a}} + \rho^{\mathrm{a}0}(\boldsymbol{b}-\boldsymbol{a}^{\mathrm{s}})\right\} \tag{5}$$

where $\boldsymbol{v}^{\mathrm{ws}}$ and $\boldsymbol{v}^{\mathrm{as}}$ are the relative velocities of water $\boldsymbol{v}^{\mathrm{w}}$ and air $\boldsymbol{v}^{\mathrm{a}}$ to solid velocity $\boldsymbol{v}^{\mathrm{s}}$; p^{w} and p^{a} are the water and air pressures; k^{w} and k^{a} are the permeability coefficients of water and air.

The constitutive equations for the compressibility of water and air phases under the barotropic condition are expressed as

$$\frac{1}{\rho^{\mathrm{w}0}}\frac{\partial\rho^{\mathrm{w}0}}{\partial t} = \frac{1}{K^{\mathrm{w}}}\frac{\partial p^{\mathrm{w}}}{\partial t} \tag{6}$$

$$\frac{1}{\rho^{\mathrm{a}0}}\frac{\partial\rho^{\mathrm{a}0}}{\partial t} = \frac{1}{K^{\mathrm{a}}}\frac{\partial p^{\mathrm{a}}}{\partial t} \tag{7}$$

where K^{w} and K^{a} are the bulk moduli of water and air.

2.2. Elastoplastic constitutive model

The constitutive equations for soil skeleton of the unsaturated soil were based on a simplified elastoplastic model for saturated sandy soil (Mori et al., 2011; Matsumaru and Uzuoka, 2016).

Same as the previous studies (Laloui et al., 2016; Switala and Wu, 2018; Sitarenios et al., 2021; Liu et al., 2020), the generalized Bishop's stress formula was adopted to define the effective stress $\boldsymbol{\sigma}'$ with the degree of water saturation s^{w} as the weighting factor to characterize the unsaturated soil behavior. The expression is given by

$$-\boldsymbol{\sigma}' = -\boldsymbol{\sigma} - p^{\mathrm{a}}\boldsymbol{I} + s^{\mathrm{w}}p^{\mathrm{c}}\boldsymbol{I} \tag{8}$$

where p^{c} is the matric suction defined as the difference between air pressure p^{a} and water pressure p^{w}; $\boldsymbol{I}$ is the second-order unit tensor. In this paper, the stress vector is considered as tension positive while pore fluid pressure compression positive.

The yield function, hardening rule, plastic potential, and elastic moduli were supplemented in Appendix. It is worth mentioning that the kinematic hardening rule is adopted in the constitutive stress–strain model, with shear strain dependent plastic shear modulus reduction law. Since difference phases (shaking and rainfall) were considered in this study, this law could account for the shaking-caused modulus reduction for the following analysis of slope response to rainfall.

2.3. Water retention constitutive model

Soil–water characteristic curve (SWCC) describes the relationship between the degree of saturation s^{w} and suction p^{c} and is described by the VG model (van Genuchten, 1980) as

$$s_{\mathrm{e}}^{\mathrm{w}} = \frac{s^{\mathrm{w}} - s_{\mathrm{r}}^{\mathrm{w}}}{s_{\mathrm{s}}^{\mathrm{w}} - s_{\mathrm{r}}^{\mathrm{w}}} = \left[1 + (ap^{\mathrm{c}})^{n}\right]^{-m} \tag{9}$$

where $s_{\mathrm{e}}^{\mathrm{w}}$ is the effective degree of saturation; $s_{\mathrm{r}}^{\mathrm{w}}$ and $s_{\mathrm{s}}^{\mathrm{w}}$ are the residual and saturated degrees of saturation; a, n, and m are the material parameters. Note that unlike other work (Gallipoli et al., 2003; Tarantino, 2009; Muraleetharan et al., 2009; Hu et al., 2013; Zhang and Muraleetharan, 2019) on the dependence of SWCC of soil deformation, the SWCC here was not directly coupled with soil deformation or volume changes, which could have an impact on the results of the following simulations. However, the SWCC model in Eq. (9) could reasonably represent the water retention behavior of unsaturated soil, and it was still adopted elsewhere (Ehlers and Ammann, 2004; Laloui et al., 2016; Liu et al., 2020; Cuomo et al., 2021; Sitarenios et al., 2021).

The permeability coefficient functions (PCF) of water and air in the VG model depend on the effective saturation and take the forms of

$$k^{\mathrm{w}} = k_{\mathrm{s}}^{\mathrm{w}}\left(s_{\mathrm{e}}^{\mathrm{w}}\right)^{\zeta}\left\{1 - \left[1 - \left(s_{\mathrm{e}}^{\mathrm{w}}\right)^{1/m}\right]^{m}\right\}^{2} \tag{10}$$

$$k^{\mathrm{a}} = k_{\mathrm{s}}^{\mathrm{a}}\left(1 - s_{\mathrm{e}}^{\mathrm{w}}\right)^{\eta}\left[1 - \left(s_{\mathrm{e}}^{\mathrm{w}}\right)^{1/m}\right]^{2m} \tag{11}$$

where $k_{\mathrm{s}}^{\mathrm{w}}$ and $k_{\mathrm{s}}^{\mathrm{a}}$ are the saturated permeability coefficients of water and air; ζ and η are the material parameters.

2.4. Numerical implementation in FEM formulation

The weak forms of Eqs. (2)–(5) were obtained using the Galerkin method of weighted residuals and implemented in the finite element formulation. The Newton-Raphson method was applied to linearize and solve the weak forms with three primary variables, i.e., solid acceleration $\boldsymbol{a}^{\mathrm{s}}$, pore water pressure p^{w}, and pore air pressure p^{a}. Eight-node element was adopted in FEM, where displacement is approximated at eight nodes and fluid pressures four nodes. Newmark integration scheme was used for time discretization in the seismic analysis. The convergence tolerance was 1×10^{-9}.

2.5. Calibration of constitutive models

The calibration of constitutive models mainly involved the response of the soil to monotonic and cyclic loading, as well as the hydraulic properties.

The soil used in the centrifuge experiments is silty sand having a particle size range of 0.01 mm–4 mm and fines content of about 10%, and the uniformity coefficient and curvature coefficient are 7.46 and 1.01. The slope made of the soil has a relative density of 85% and a void ratio of 0.75.

Undrained monotonic and cyclic triaxial tests on the soil specimens were conducted and the simulated results were compared with the experimental results. Fig. 1 plots the results of laboratory tests on saturated specimens in simulations and experiments. Both the stress–-strain curve and effective stress path during monotonic and cyclic show good consistency between simulations and experiments. The stress–-strain curve and stress path curve in Fig. 1(a) and (b) at the initial stage were quite linear, which is slightly different from the experimental results, whereas the simulation results of the cyclic triaxial test in Fig. 1(c) and (d) show a much better performance. Since both cyclic and monotonic element test simulations adopted the same hardening law about the strain-dependent shear modulus reduction, the performance of the element simulations might be slightly different. However, the main features and general trends of the results could be reproduced using the element simulation of the monotonic triaxial test. The elastoplastic parameters of the soil are given in Table 1.

The results of SWCC and PCF attained from laboratory tests (Xu et al., 2022) and van Genuchten (1980) model are presented in Fig. 2. The comparison between experimental results and the VG model shows that the mathematical equations in the VG model employed in the hydro-mechanical analysis framework are capable of capturing the hydraulic characteristics of soil.

3. Numerical modeling

3.1. Finite-element (FE) model

The two-dimensional FE model in Fig. 3 is adopted for numerical analysis and consists of three parts, which are soil, void, and base. The model had the same geometry as the one represented by the centrifuge experiments (Xu et al., 2022) so that the results from simulations could be compared with those from experiments. In the figure, several nodes and elements used for the later discussions are labeled. M1–M3 are nodes for displacement analysis; N1 (P1)–N5 (P5) are nodes for pore water pressure analysis; E1–E5 are elements for stress path analysis.

Table 2 provides the simulation program with four cases. Cases A1 and B1 were the baseline simulations to check the slope response to rainfall. Cases A2 and B2 were simulated to examine the slope response to shaking and the following rainfall with different intensities.

The soil material had most of the parameters of the effective

Table 1
Elastoplastic parameters of saturated soil specimen.

Parameter	Value
Non-dimensional bulk moduli, K^* and G^*	1500 and 600
Kinematic hardening parameters, a_0, $a_{\min}$, C_{ref}, $p_{\mathrm{ref}}^{\mathrm{c}}$, and b	1300, 48, 5000, 1 kPa, and 1.63
Elastic region k and critical stress ratio M	0.01 and 1.63
Dilatancy d_0	0.02

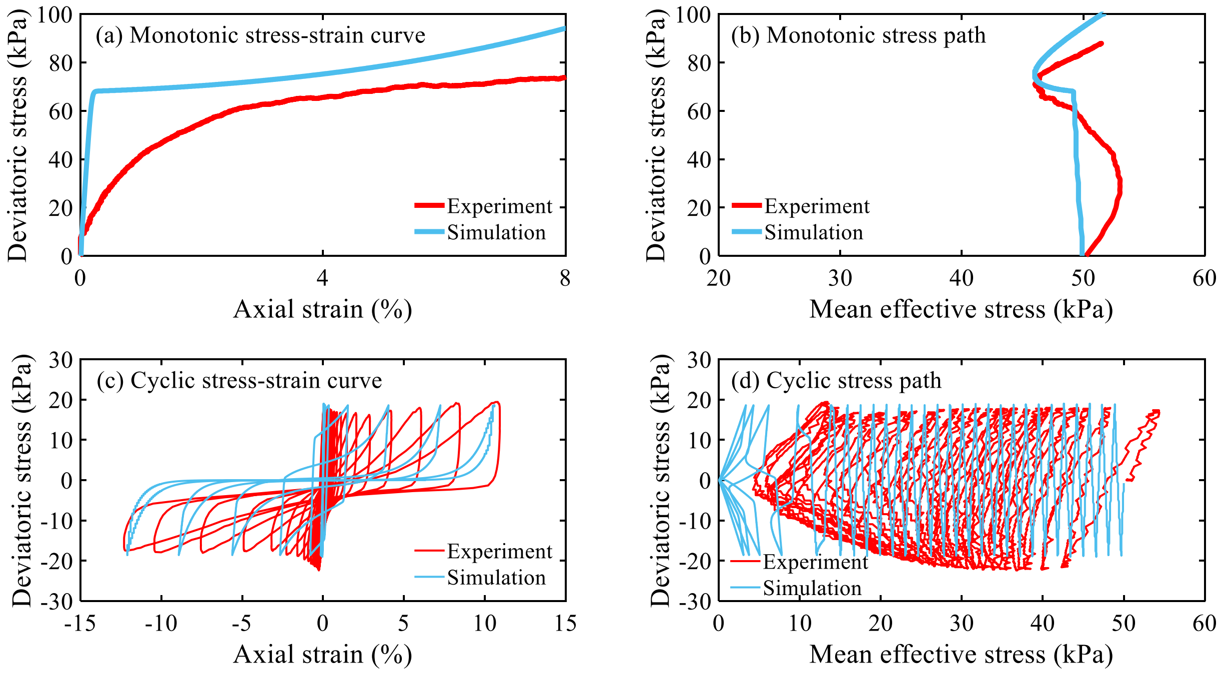

Fig. 1. Undrained monotonic and cyclic triaxial tests on soil specimens.

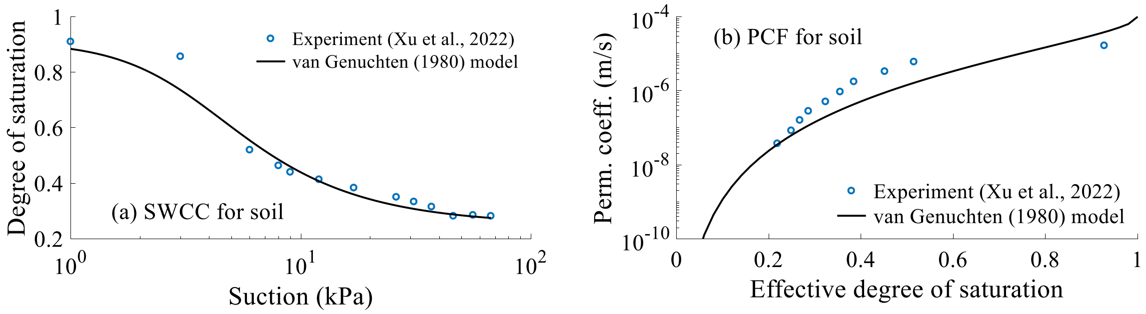

Fig. 2. SWCC and PCF for soil.

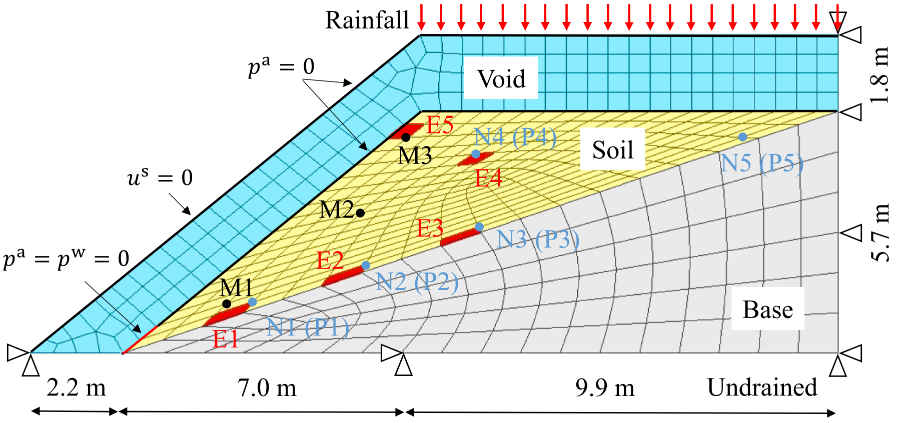

Fig. 3. Two-dimensional FE model.

Table 2
Numerical simulation program.

Case	Condition for slope	Shaking intensity	Rainfall intensity
A1	Heavy rainfall	None	30 mm/h
B1	Light rainfall	None	9 mm/h
A2	Shaking and then heavy rainfall	4.6 m/s^2	30 mm/h
B2	Shaking and then light rainfall	4.6 m/s^2	9 mm/h

stress–strain relationship based on the triaxial tests on saturated soil specimens in Table 1. For the unsaturated soil, parameters of the plastic shear modulus related parameter C_{ref} and dilatancy parameter d (see Appendix) were calibrated by comparing the distribution of equivalent strains caused by shaking between simulation and experiment. The void material had a linearly elastic stress–strain relationship. The base material had a linearly elastic stress–strain relationship with large Lame's constants, as well as permeability much lower than soil permeability. The mechanical parameters of soil, void, and base materials are given in Table 3.

The void material was simulated by aerial elements (Uzuoka et al., 2008; Mori et al., 2011), which were essentially soil elements but were treated specially for the purpose of smooth infiltration during rainfall in the simulations. The void elements were also used to model the surface runoff, which was observed in the centrifuge experiments. Although it was not significant, using the void elements could make the simulation closer to the experimental condition. The linearly elastic stress–strain model with small moduli was assigned to the void with porosity of unity and soil particle density of zero. As to the displacement boundary, all the nodes of the aerial elements were fixed so that the elements would not move during the analysis.

Table 3
Mechanical parameters of soil, void, and base materials.

Material	Parameter	Value
Soil	Non-dimensional bulk moduli, K^* and G^*	1500 and 600
	Kinematic hardening parameters, a_0, a_{min}, C_{ref}, $p_{\mathrm{ref}}^{\mathrm{c}}$, and b	1300, 48, 7700, 1 kPa, and −1.63
	Elastic region k and critical stress ratio M	0.01 and 1.63
	Dilatancy, d_0 and d_{min}	0.10 and 0.10
Void	Lame's constant λ_0	10 kPa
	Lame's constant μ_0	1 kPa
Base	Lame's constant λ_0	24 GPa
	Lame's constant μ_0	16 GPa

Fig. 4 plots the SWCC and PCF of the void. The VG model was adopted to describe the SWCC of void elements, with the same expression in Eq. (9). The PCF of water and air adopts the power law (Mori et al., 2011), with expressions of

$$k^{\mathrm{w}} = k_{\mathrm{s}}^{\mathrm{w}} \left(s_{\mathrm{e}}^{\mathrm{w}}\right)^{\zeta} \tag{12}$$

$$k^{\mathrm{a}} = k_{\mathrm{s}}^{\mathrm{a}} \left(1 - s_{\mathrm{e}}^{\mathrm{w}}\right)^{\eta} \tag{13}$$

Table 4 contains the SWCC and PCF parameters of soil and void materials used in the numerical simulations.

3.2. Initial slope condition

The simulations in four cases were performed in different stages, but the self-weight analysis was conducted before the analysis with rainfall or shaking. The nodes of all void elements were fixed, but the nodes along the surface boundary of soil slope were free to move; the nodes along the bottom boundary of the base were fixed in the horizontal and vertical directions, and the nodes along the vertical boundary of the base were fixed in the horizontal direction. The air pressures of all nodes of void elements were set as zero. The water pressures of three nodes, which were along the soil slope surface and started from the slope toe, were set as zero. The boundary conditions are shown in Fig. 3. The time

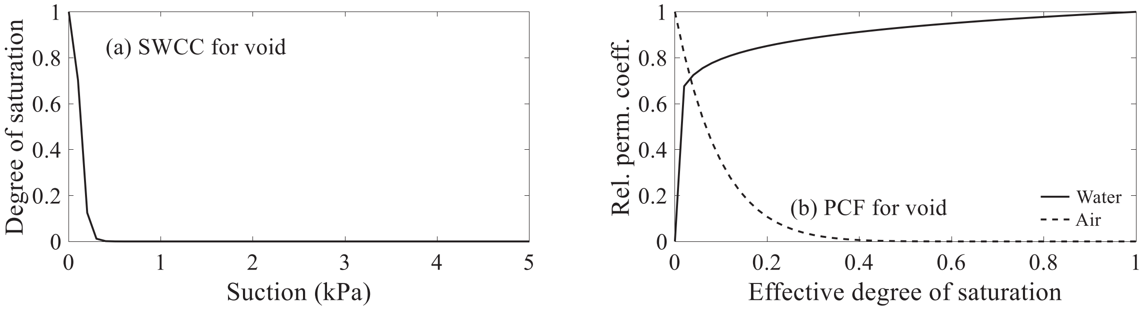

Fig. 4. SWCC and PCF of void.

Table 4
SWCC and PCF parameters of soil and void materials.

Material	Degrees of saturation, S_r^w and S_s^w	Permeability coefficients, k_s^w and k_s^a	a, n, and m	ζ and η
Soil	0.21 and 0.95	6.5×10^{-5} m/s and 6.5×10^{-6} m/s	0.42 kPa^{-1}, 2.1, and 0.52	0.50 and 0.33
Void	0 and 1	6.5×10^{-4} m/s and 6.5×10^{-5} m/s	5 kPa^{-1}, 3 and 3	0.1 and 10

increment for calculation was 0.001 s; the coefficient in the time discretization was 0.6, which was the same as the coefficient γ in the Newmark integration method. In this process, desaturation continued while suction and effective stress kept growing. Since the numerical model had the geometry taken after the centrifuge model and the same increasing "gravity" process was assigned to the numerical model, the numerical model could reproduce the initial condition as the one in the centrifuge model. The slope condition after self-weight analysis was used for all four cases. Fig. 5 shows the distributions of suction and effective stress in the slope after self-weight analysis.

3.3. *Response of slope to rainfall*

Simulations A1 and B1 were carried out to assess the general performance of the FE slope model subjected to rainfall. After the self-weight analysis, rainfall infiltration was started in the model. The displacement boundary condition was the same as the boundary condition in the self-weight analysis. The rainfall flux was applied to the nodes along the upper horizontal surface of the void, which was consistent with the rainfall condition in experiments. A total of 21 nodes covered the horizontal surface 9.9 m in length, so the nodal flux in each node was calculated with the rainfall intensity. The air pressures of all nodes of void elements were zero. The water pressure boundary was the same as the one in the self-weight analysis. The time increment for calculation was 0.001 s; the coefficient in the time discretization was 0.6, which was the same as the coefficient γ in the Newmark integration method. The pore water pressure and soil deformation in terms of equivalent (deviatoric) strain were analyzed using results from numerical simulations and centrifuge experiments.

Pore water pressures of N1–N5 in the FE model and their counterparts P1–P5 in the centrifuge model during rainfall, as well as the pore air pressure of N1–N5 in the FE model, are compared in Fig. 6. For slopes during rainfall without prior shaking, the time when positive pore water pressures started to develop was well reproduced, as seen in the slight difference between the simulation result and experimental result. However, N2–N4 in Fig. 6(a) and (b) show notable deviations in the growing trends during rainfall, which may result from the water pressure boundary imposed on the slope model. Since zero water pressure value was given to several nodes around the toe of the slope, it could be different from the condition in the experiment and cause the disparity. Additionally, the pore air pressures in Fig. 6(c) and (d) are quite small and do not show much variety despite the difference in the rainfall intensity. It could result from the initial pore air pressure boundary given to the slope. Since zero pore air pressure was designated along the surface of the soil slope, the pore air pressure in the slope such as N1–N5 in Fig. 6(c) and (d) became insignificant. It suggested that the effect of air flow in both simulations was insignificant. According to Hu et al. (2016), the air flow had a delaying effect on the wetting process during rainfall infiltration and the overestimated slope deformation would be produced when the air flow was neglected. Therefore, in cases A1 and B1, the air flow was unlikely to make a significant impact on the wetting process but might overestimate the slope deformation during rainfall.

Slope deformation is described by the equivalent strain and volumetric strain with definitions of

$$\varepsilon_d = \sqrt{\frac{2}{3}}\sqrt{\left(\varepsilon_{xx} - \frac{\varepsilon_v}{3}\right)^2 + \left(\varepsilon_{yy} - \frac{\varepsilon_v}{3}\right)^2 + \left(\varepsilon_{zz} - \frac{\varepsilon_v}{3}\right)^2 + 2\varepsilon_{xy}{}^2 + 2\varepsilon_{yz}{}^2 + 2\varepsilon_{zx}{}^2} \tag{14}$$

$$\varepsilon_v = \varepsilon_{xx} + \varepsilon_{yy} + \varepsilon_{zz} \tag{15}$$

where ε_{xx}, ε_{yy}, and $2\varepsilon_{xy}$ are the strain components on the *xy* plane; the strain components ε_{zz}, ε_{yz}, and ε_{zx} are all zero, given the plane strain condition. As for the strains from experiments, the image analysis was conducted to get the soil displacement in the centrifugal model, based on which all strain components in the divided small soil elements were obtained using the calculation method in Xu et al. (2022), and the incremental equivalent and volumetric strains were then calculated according to Eqs. (14) and (15).

The incremental equivalent strain of slope caused by in cases A1 and

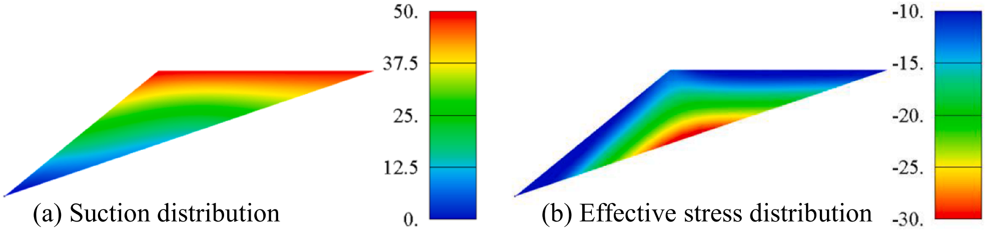

(a) Suction distribution

(b) Effective stress distribution

Fig. 5. Distributions of suction (a) and effective stress (b) in slope after self-weight analysis (unit: kPa).

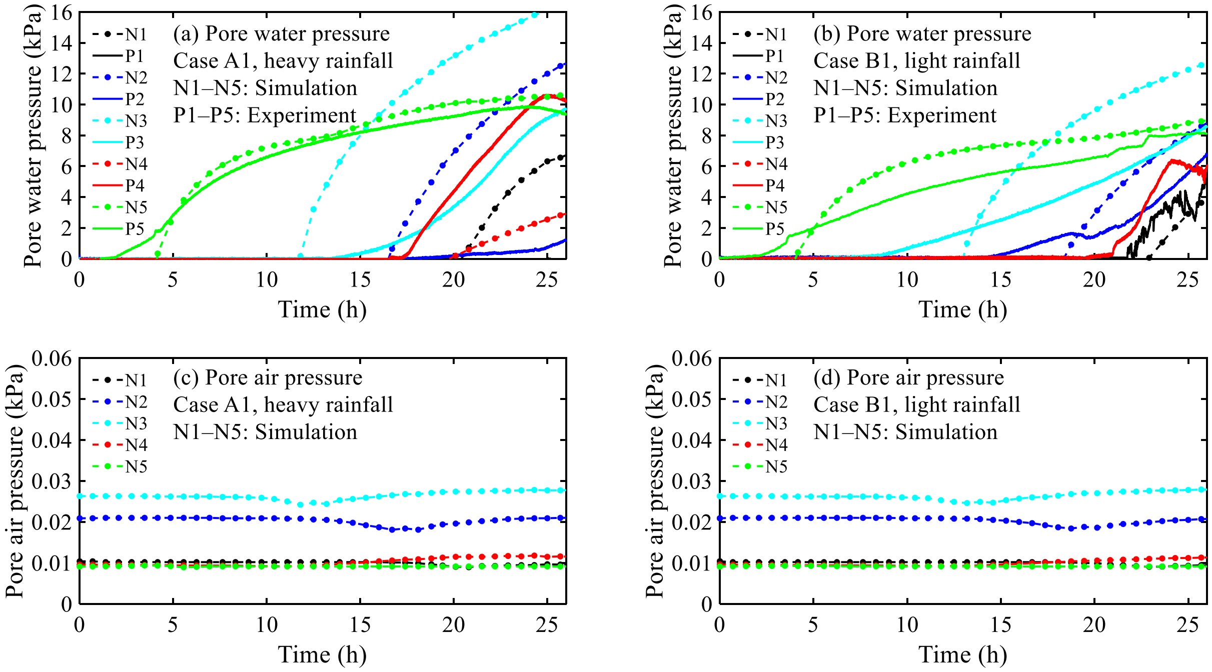

Fig. 6. Pore water/air pressure response of slopes to rainfall in cases A1 and B1 (experimental data from Xu et al., 2022).

B1 is displayed in Fig. 7, showing the slope deformation upon rainfall-induced failure. The localization of deformation was represented by the concertation of strains, which also indicated the slip surface within the slope. With respect to the deformation pattern of the slopes during heavy rainfall in case A1, Fig. 7(a) and (c) show close similarities in the location of the slip surface and the strain level. As to the slope subjected to light rainfall in case B1, the deformation difference between simulation and experiment in Fig. 7(b) and (d) is negligible since the general deformation at the onset of failure is small. In addition, the slope failure initiation time in simulation is comparable to the experimental failure initiation time as given in the figures. Therefore, the slope deformation under rainfall with different intensities was well reproduced.

The FE model with the determined material parameters could be used to simulate the response of slope to rainfall as the general hydro-mechanical behavior of the slope was captured in the simulations.

3.4. *Response of slope to shaking*

The shaking analysis of slopes in cases A2 and B2 was conducted before the rainfall analysis. The input motion is given in Fig. 8, which is also the same motion applied to the centrifuge experiments. The motion had a frequency of 1 Hz and an intensity of 4.6 m/s^2. All nodes of void elements were fixed, but the nodes along the surface boundary of soil slope were free to move; the air pressures of all nodes of void elements were set as zero. The input motion was given to the nodes at the boundary of the base. The water pressure boundary was the same as those in the self-weight and rainfall analyses. The time increment for calculation was 0.00002 s; the coefficients for the Newmark integration

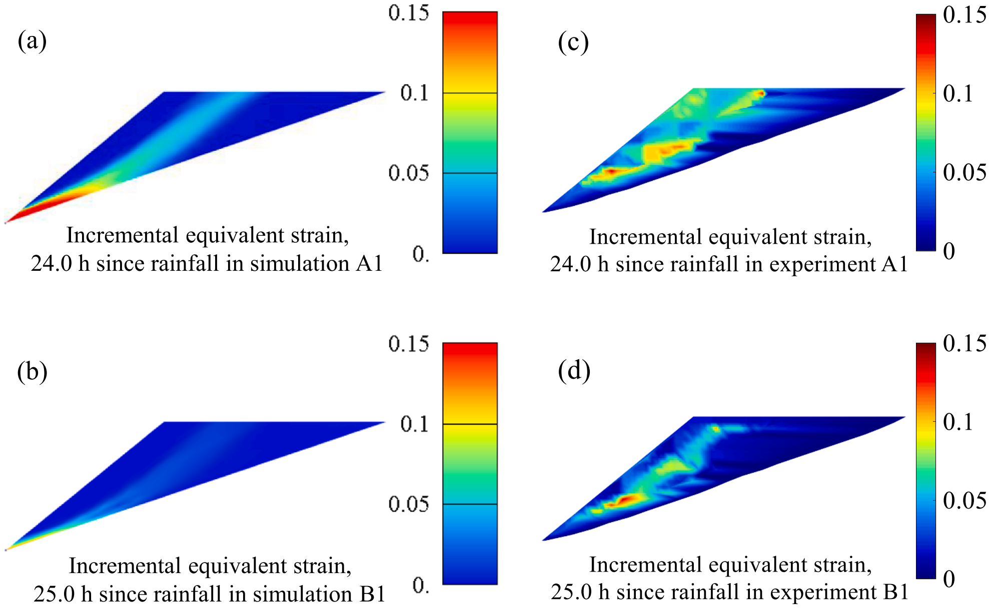

Fig. 7. Equivalent strains upon rainfall-induced landslides in simulations A1 (a) and B1 (b) and experiments A1 (c) and B1 (d).

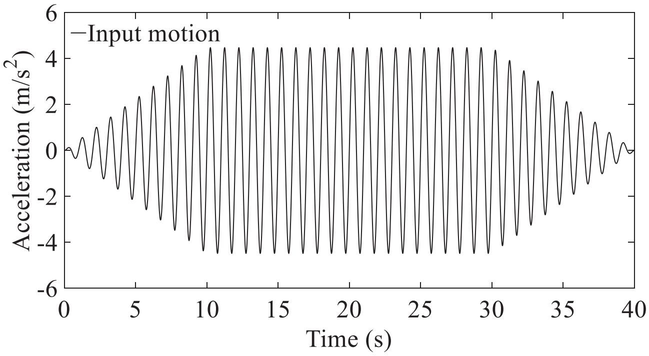

Fig. 8. Input motion in the seismic analysis in cases A2/B2.

method were $\gamma = 0.6$ and $\beta = 0.3025$.

Slope deformation was obtained with the adjusted parameters (see Table 3) based on the calibration using the shaking tests. Fig. 9 demonstrates the shaking-induced incremental equivalent and volumetric strains in slopes in simulations A2/B2 and experiments A2 and B2. Despite the inability of FEM to simulate the crack generation in the slope, the simulated result shows the shaking-induced slope deformation in terms of the slip surface location and the incremental equivalent strain magnitude in Fig. 9(a), (c), and (e). Starting from the toe to the crest, the slip surface in Fig. 9(a) is quite close to the slope surface, which is also observed in experiments A2 and B2. Moreover, both simulations and experiments report the largest deformation at the lower part of the slopes and the decreasing deformation as the height of the soil grew. Although the incremental volumetric strain is not fully produced as the magnitude in the simulation in Fig. 9(b) is smaller than those in experiments in Fig. 9(d) and (f), the location of the incremental volumetric strain is roughly indicated in the simulation.

One noteworthy point is that, since shaking-induced soil compression in Fig. 9(b) causes the void ratio to reduce and thus an increase in the degree of saturation, it will reduce the effective stress and induce more soil deformation. Thus, the SWCC without the coupling of soil deformation could underestimate the soil deformation during shaking. Investigation of the coupling between SWCC and soil deformation (Muraleetharan et al., 2009; Zhang and Muraleetharan, 2019) is needed to quantitatively evaluate the slope deformation.

4. Updated FE model incorporating the effect of shaking

4.1. Effects under consideration

The rainfall analyses in cases A1 and B1, as well as the shaking analyses in cases A2 and B2 have been completed now. The results have verified that the FE model could be applied to simulate slope deformation under rainfall and earthquake. However, the effect of an earthquake on the slope response to the subsequent rainfall should be considered if the post-earthquake rainfall analysis was to be continued.

As shown in Fig. 9(a), shaking in simulations A2/B2 induces large shear strain along the slip surface of the slope. One factor that would affect the response of slope to the rainfall after shaking was the shaking-induced shear modulus degradation. Previous research (Vucetic and Dobry, 1991; Oka et al., 1999; Kramer, 1996; Towhata, 2008; Upreti and Leong, 2021) on the cyclic response of soil has shown that the plastic shear modulus reduced with the cyclic shear strain. This would influence the hydro-mechanical behavior of slope subjected to the following rainfall and thus needed to be considered in the following post-shaking rainfall analysis.

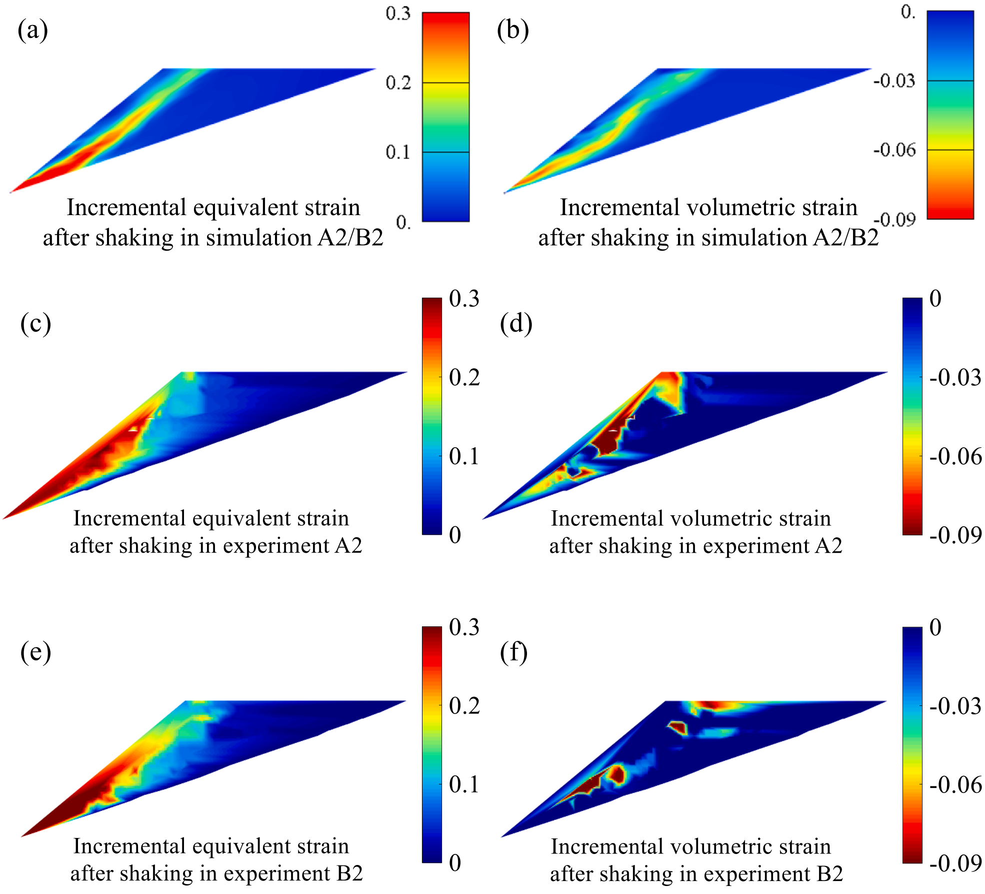

Incremental equivalent strain after shaking in simulation A2/B2

Incremental volumetric strain after shaking in simulation A2/B2

Incremental equivalent strain after shaking in experiment A2

Incremental volumetric strain after shaking in experiment A2

Incremental equivalent strain after shaking in experiment B2

Incremental volumetric strain after shaking in experiment B2

Fig. 9. Slope deformation caused by shaking in simulations A2/B2, (a) and (b), and the corresponding experiments, (c)–(f).

In Eq. (22) in the Appendix, parameter a, which relates to the plastic shear modulus, degrades as the shearing increases. In the shaking analysis, continual increment of deviatoric strain would cause the parameter a to reduce. The contribution of shaking-induced equivalent strain (Fig. 9(a)) to the degradation of the shear modulus of soil was reflected by Eq. (22). With the application of this equation, the effect of plastic shear modulus reduction could be assessed in the numerical simulation.

As shown in Fig. 9(b), shaking in simulations A2/B2 induces negative volumetric strain in the slope along the shear band. It indicated compression and thus decreased permeability, which could cause severe deformation during the following rainfall. Thus, the feature of permeability reduction in the deformation soil should be considered in the post-shaking rainfall simulation. According to the Kozeny–Carman equation (Kozeny, 1927; Carman, 1937; Chen et al., 2021), the saturated permeability coefficient K_s of soil after volume change was empirically estimated based on the void ratio e_0 of the soil. The common form of the equation is $K_s = C\frac{e^3}{1+e}$, where C is a parameter dependent on soil type and particle characteristics. Therefore, when C is constant, the saturated permeability coefficient $K_s^{'}$ under a certain level of volumetric strain ε_v is established as

$$\frac{K_s^{'}}{K_s} = \frac{\left[e + \varepsilon_v(1+e)\right]^3}{e^3(1+\varepsilon_v)} \tag{16}$$

Another feature of the slope after shaking was the crest cracks near the slope shoulder, as observed in the experimental results (Xu et al., 2022), e.g., Fig. 9(c) and (e). Since the direct measurement of permeability associated with cracks is difficult, the usual approach is to adopt empirical values (Li et al., 2011; Zhang et al., 2020) or to calculate the value when the crack geometry is known (Childs, 1969; Olivella and Alonso, 2008; Maleki and Pouya, 2010). Neither approach is applicable to this simulation. To describe the effect of shaking-induced surface cracks on the permeability enhancement, this study adopted a concept of damage (Lu et al., 2013; Pogacnik et al., 2014; Gao et al., 2021). The crack width is assumed to be an S-shaped function of depth (Zhang et al., 2014; Gao et al., 2021) and the width of crack decrease as the depth of soil increases. Here, by reference to Gao et al. (2021), the damage parameter D is taken as

$$D = 1 - \frac{1}{1 + e^{-s(h-h_0)}} \tag{17}$$

where h is the depth within which soil is considered to be cracked and it is taken as 1.5 m based on the observation from the centrifuge experiment; h_0 is the midpoint depth, which is 0.75 m; s is the parameter controlling the steepness of the curve and is taken as 2.

The distribution of damage parameter D is plotted in Fig. 10. D gradually decreases from about 0.8 to 0.2 as the depth of the soil from the slope crest grows. The soil at the surface is the most damaged and the damage effect reduces with the depth of soil.

After the damage parameter D is defined, the effect of damage on permeability and strength is described by

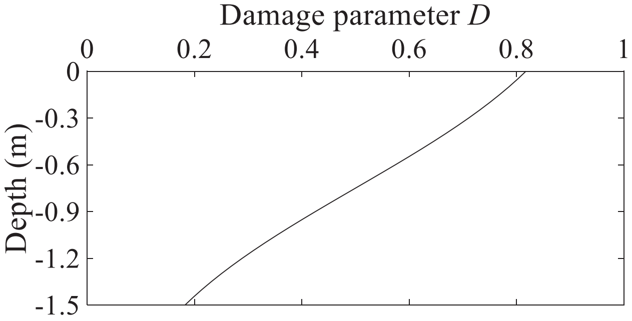

Fig. 10. Distribution of damage parameter D along soil depth.

$$K_s^D = K_s/(1-D) \tag{18}$$

$$\varphi^D = \varphi \times (1-D) \tag{19}$$

where K_s^D and φ^D are the saturated permeability coefficient and angle of friction associated with shaking-induced damage.

The distribution of saturated permeability coefficients on the basis of shaking-caused compression and damage is illustrated in Fig. 11. First, Eq. (16) was applied to each element after the shaking-induced volumetric strain was obtained from the analysis; thus, the distribution of saturated permeability coefficients after shaking was known, as plotted in the slope model with a color bar indicating the reduced values in Fig. 11. The largest reduction in permeability coefficient is about 0.6 times the original value K_s. Second, since the constitutive model for cracks was not incorporated in the simulation, the generation of cracks attributed to shaking would not be directly obtained here. However, as the main purpose was to examine the effect of shaking-induced damage (cracks) on the slope response to the subsequent rainfall, the location of the damage zone could be determined with some simplifications, such as by referring to the strain distributions in Fig. 9. The soil within the shear band in Fig. 9(a) near the slope crest was selected as the damaged soil; thus, the width of the damage zone was determined and it was about 2.5 m as indicated by the length of the upper side of the red quadrilateral in Fig. 11. The manner to decide the crack location was reasonable since the earthquake-induced cracks were usually found near the slope shoulder (Kobayashi, 1971; Usui et al., 2013). Meanwhile, the observed crack in the experiment (Xu et al., 2022) was about 1.5 m in depth, at which the shaking-induced equivalent strains in Fig. 9(c) and (d) along the slip surface were also similar to their simulated counterpart in Fig. 9 (a). Therefore, the crack depth of 1.5 m was used in the numerical simulation. The permeability coefficient and angle of friction of soil in the damage zone were determined based on Eqs. (17)–(19). The calculation of the depth of earthquake-induced crack was not widely available since it was greatly affected by slope configuration, earthquake intensity, soil properties, etc. Because currently the depth could not be directly determined from the simulation result, the observation from the centrifuge experiment was referred to for the purpose of the crack depth estimation. As introduced earlier, many studies of the crack-containing slope under rainfall (Wang et al., 2011; Zeng et al., 2020; Zhang et al., 2020) did not consider the generation of cracks; rather, the cracks were manually set with different locations and depths in the slope. Whereas in this study the shaking simulation could provide reference for the estimation of crack location based on the strain distribution, such as the

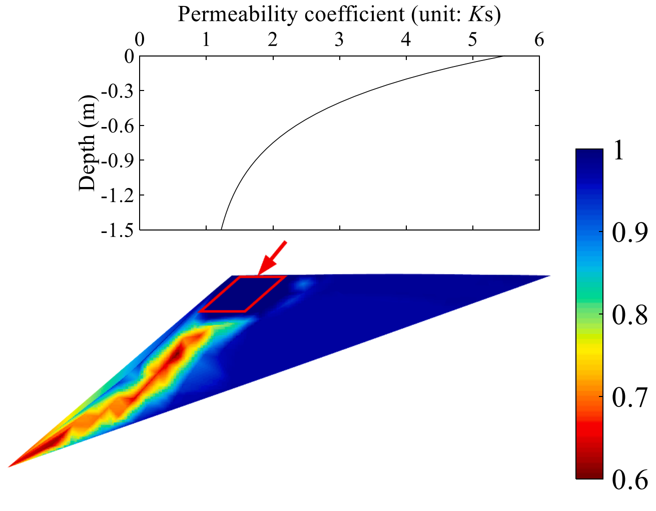

Fig. 11. Distribution of saturated permeability coefficients after shaking (reduction in K_s based on the Kozeny–Carman equation and increase in K_s based on the damage parameter).

incremental equivalent strain in Fig. 9(a); the determination of crack depth required both the simulation and other methods like the experimental result. Regarding the desiccation-induced crack, many studies have been conducted to estimate the depth adopting methods proposed by Morris et al. (1992), Konrad and Ayad (1997), and Lu and Likos (2004), e.g., the crack depth calculation method that assumed crack in unsaturated soil occurred when the coefficient of earth pressure at rest equaled zero (Lu and Likos, 2004), which might be used for the preliminary assessment of earthquake-induced crack depth. A more detailed and straightforward tool such as the extended finite element method will benefit this study further.

The zone surrounded by the red quadrilateral in Fig. 11 contains the damaged soil and the calculated permeability coefficients based on volumetric strains are replaced with the damage-induced coefficients ranging from approximately 1.3 K_s to 5.5 K_s according to Eqs. (17) and (18). As these large coefficients could not be indicated clearly by the color bar once they were plotted together with the reduced coefficients (less than K_s) in the slope model, the distribution of the permeability enhancement was instead plotted against the depth above the slope model in Fig. 11. Also, soil in this zone has reduced the original angle of friction by about 0.2 to 0.8 according to Eqs. (17) and (19).

4.2. Slope performance with consideration of each effect

To check the applicability of the above methods in the simulations of slope behavior during post-earthquake rainfall, this section will compare the slope deformation induced by post-earthquake heavy rainfall in case A2. The slope model with shaking-induced shear modulus reduction, permeability reduction, and damage will be used for the analysis separately so that the effect of each factor can be examined and the slope performance under each condition can be properly evaluated.

Fig. 12 contains the slope deformation in terms of equivalent strain induced by post-earthquake rainfall with the consideration of shaking-induced shear modulus reduction (a), shaking-induced permeability reduction (b), shaking-induced damage (c), and their combined effect (d).

It can be seen from Fig. 12(a) that shaking-induced shear modulus reduction influences the location of the slip surface of the slope subjected to the following rainfall and the slip moves closer to the slope surface, but the deformation mainly occurs at the lower part of the slope. The location where the rainfall-induced deformation mostly occurred in the soil that has been deformed by the previous earthquake as shown in Fig. 9a. Comparing Fig. 12(a) and Fig. 7(a) shows that once the slope is subjected to a prior earthquake, the slope deformation caused by the following rainfall is greatly changed because of the reduced shear modulus of soil.

Comparing Fig. 12(b) and Fig. 7(a) indicates that the shaking-induced permeability reduction of the soil along the slip surface does not make a significant difference in the slope failure features. This is associated with a small amount of volumetric strain, as shown in both simulation (Fig. 9(b)) and experiments (Fig. 9(d) and (f)), resulting in the largest reduction in saturated permeability coefficient of only 40% (Fig. 11) and a noticeable discrepancy between two results does not exist. However, when the shaking-induced volumetric strain is large in some cases, this effect should be considered in the analysis of slope deformation caused by rainfall after an earthquake to account for the impact of permeability change.

In Fig. 12(c), the deformation near the damage zone shows large deformation since the effect of shaking-induced soil strength reduction and permeability enhancement are included in the model, but the largest deformation still takes place around the slope toe. With the consideration of damage effect, the slip surface of the slope during rainfall was slightly changed compared with that in the homogeneous slope in Fig. 7 (a), and the failure of the damage zone is induced.

When all three factors are considered in the analysis, the slope deformation is demonstrated in Fig. 12(d). The characteristics of slope failure caused by post-earthquake rainfall became completely different from those of slope failure caused by rainfall without previous earthquakes (Fig. 7(a)). Significant deformation was induced both near the toe and slope shoulder, and the slip surface displayed a similar location to that induced by the earthquake (Fig. 9(a)). To assess the analysis with the consideration of all three effects, the following section will examine more simulated outcomes and compare them with the experimental results.

5. Response of slope to post-shaking rainfall

This section will thoroughly investigate the hydro-mechanical response of slope to post-earthquake rainfall based on the model considering the combined effect of shaking-induced shear modulus reduction, permeability reduction, and damage. Pore water pressure,

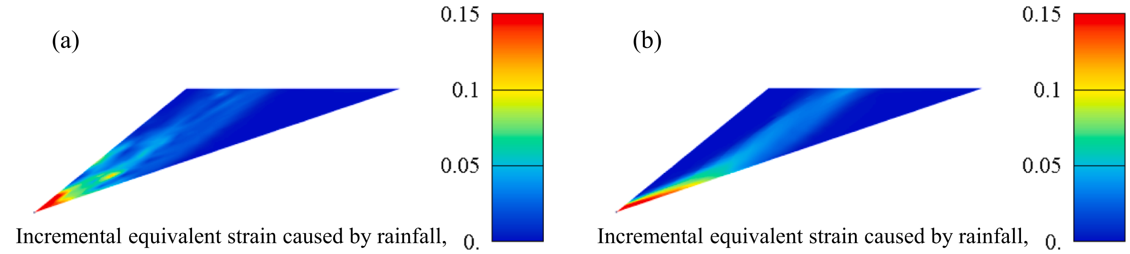

Incremental equivalent strain caused by rainfall, considering only shaking-induced modulus reduction

Incremental equivalent strain caused by rainfall, considering only shaking-induced permeability reduction

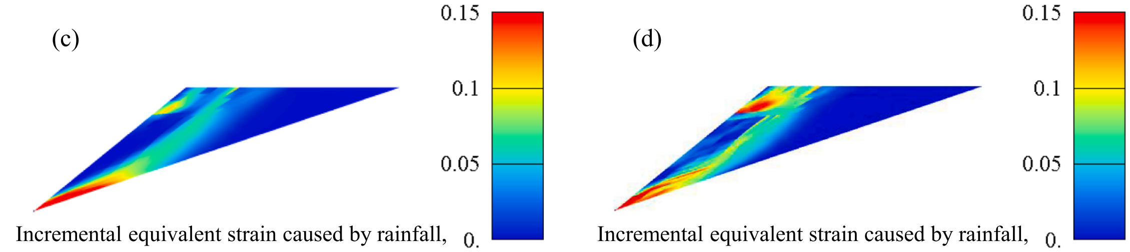

Incremental equivalent strain caused by rainfall, considering only shaking-induced damage

Incremental equivalent strain caused by rainfall, considering all three factors

Fig. 12. sloped deformation caused by post-earthquake rainfall, considering shaking-induced shear modulus reduction (a), shaking-induced permeability reduction (b), shaking-induced damage (c), and their combined effect (d).

effective stress path, slope displacement, and soil deformation during rainfall were analyzed and compared with the experimental results.

5.1. Pore water pressure

The time histories of pore water pressures during post-shaking rainfall in cases A2 and B2 are presented in Fig. 13. When subjected to heavy rainfall, the slope in simulation has a slightly different response from that in the experiment, as shown by N1 and N2 with larger values than P1 and P2. For the slope under light rainfall, however, the simulation works well to reproduce the pore water pressure response, as the simulated results match well with the experimental results, which can be seen from the initiation time of pressure build-up and increasing trend.

Due to the reduction in soil permeability along the shaking-induced slip surface, the relatively large pore water pressures were generated in the soil near the slip under rainfall after shaking, compared with the pore water pressure response of the slopes under rainfall. This could cause the effective stress to quickly drop, thus triggering slope failure near the slip.

5.2. Effective stress path

Fig. 14 plots the effective stress paths of different soil elements (Fig. 3) in slopes during rainfall. Under heavy rainfall, E1 initially exhibited an increase in its deviatoric stress and mean effective stress, resembling the consolidation process. This resulted from the increasing saturation of the above soil layer during rainfall infiltration, causing the increase in the bulk unit weight of the soil. With the increasing saturation of the soil, suction was lost and pore water pressure (N1 in Fig. 3) built up; the effective stress started to drop and the stress path moved on toward the critical state line. Deformation took place in this process. As the effective stress continued to approach the critical state line, the soil would experience excessive deformation and failure could occur. Throughout the rainfall infiltration, E5 kept shifting its stress path toward the left corner of the graph and the effective stress declined to a very low level. Since the effect of shaking-induced damage on the strength of soil near the slope shoulder was considered, water infiltration could easily cause soil deformation to develop around this area.

In the infiltration process, the stress path of E4 kept advancing and finally reached the critical state line in the end. Since E4 was close to the damaged soil, it gradually reached the critical state line and deformation of soil nearby could also develop to a larger amount. E2 and E3, however, were still at high stress levels despite continuous loss in the effective stress while shifting toward the left-hand side of the graph.

Under light rainfall, the stress paths in soil elements resembled those at the early stage of heavy rainfall. Although E1 and E4 had not reached the critical state line yet, the continual decrease in their mean effective stresses could still induce certain deformation. E5, however, had a large reduction in its effective stress since the beginning of rainfall.

Comparison of the effective stress path between simulations A2 and B2 in Fig. 14 indicates that deformation of soil near E1 and E4 during heavy rainfall is much more serious than that during light rainfall and the soil in the shaking-induced damage area represented by E5 can have considerable deformation due to water infiltration. To further examine the soil deformation induced by rainfall, the next subsection will analyze the development and distribution of equivalent (deviatoric) strains in the slope.

5.3. Slope deformation

Fig. 15 reports the equivalent strains of five soil elements E1–E5 during post-earthquake rainfall. Corresponding to their stress path progression, elements such as E1, E4, and E5 that moved toward the critical state line showed large strains. Comparison of the equivalent strains between simulations A2 and B2 in Fig. 15 illustrates that the deformation upon slope failure during heavy rainfall has a slip surface near E1, E2, and E4, and the deformation represented by the equivalent strains is more serious than that during light rainfall.

The incremental equivalent strains at the onset of rainfall-induced landslides in simulations and experiments (A2 and B2) are provided in Fig. 16. The previous analysis shows that after the slope deformation and damage are caused by the earthquake (Figs. 9–11) and under the following rainfall, the increase in the pore water pressure (Fig. 13) causes the continual reduction in the effective stress of soil (Fig. 14), contributing to the slope failure reported in Fig. 16.

Due to the incorporation of damage-induced strength reduction, the slope under heavy rainfall in simulation A2 shows large deformation in the damage zone in Fig. 16(a). This is consistent with the experimental result in Fig. 16(c), where the deformation upon slope failure is the largest in the soil near the slope shoulder and below the surface crack, as shown by the red color contour at the intersection between the slip surface and vertical crack wall in Fig. 16(c). This feature made the failure of the slope with surface cracks under heavy rainfall differ from the typical failure of slope as illustrated in Fig. 9(a). Moreover, the location of the slip surface along which the slope failed was reproduced in the simulation. Since the effect of shaking was considered, the slip surface became different from the one in the homogeneous slope in Fig. 9(a). As presented in the simulation and experimental results, the slope subjected to post-shaking rainfall had a very similar slope failure mode, thus showing that the shaking-induced deformation affected the features of a landslide caused by the subsequent rainfall, such as the location of the slip surface and the magnitude of strain along it.

As for the slopes under light rainfall in Fig. 16(b), due to rainfall infiltration and permeability increase in the soil near the slope shoulder, the suction of the soil decreased quickly, causing the effective stress to drop considerably. Since the angle of friction of soil near the slope shoulder was reduced due to damage, the dropping effective stress promoted fast yielding and large deformation. This led to the early failure of soil in this zone during infiltration. Although this feature was not significant in the experimental result in Fig. 16(d), the general slope failure pattern was similar to that in the experiment. As displayed in Fig. 16(b) and (d), the slope in either experiment or simulation had a

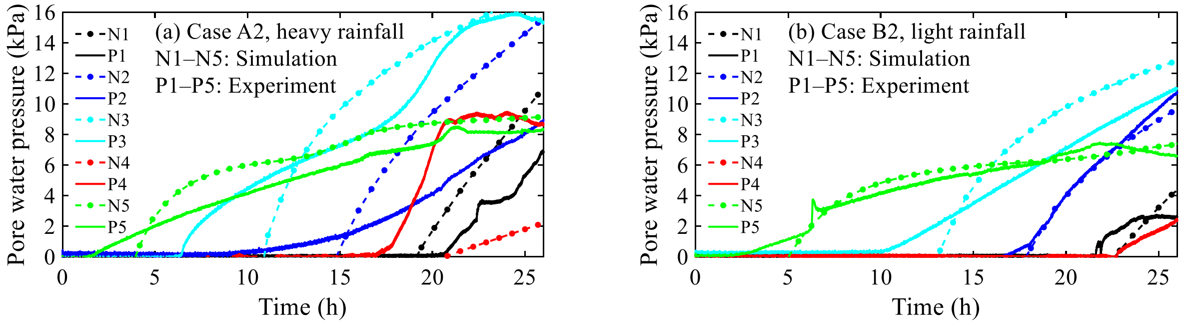

Fig. 13. Pore water pressure response of slopes to post-shaking rainfall in cases A2 and B2 (experimental data from Xu et al., 2022).

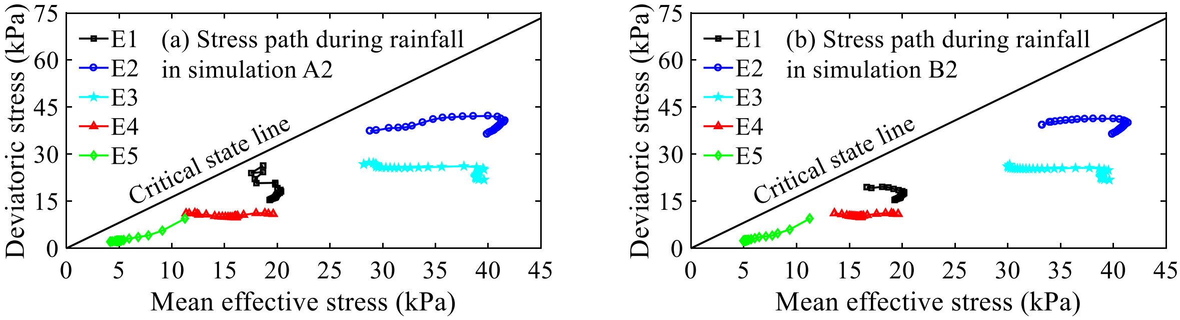

Fig. 14. Effective stress paths during rainfall in simulations A2 and B2.

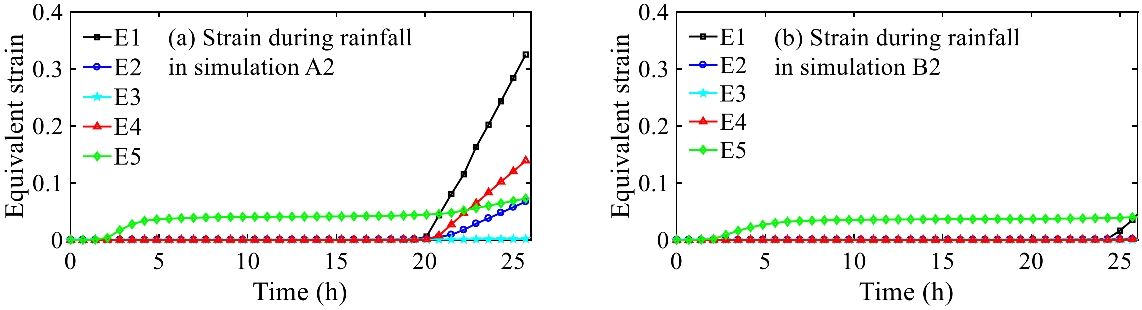

Fig. 15. Equivalent strains during rainfall in simulations A2 and B2.

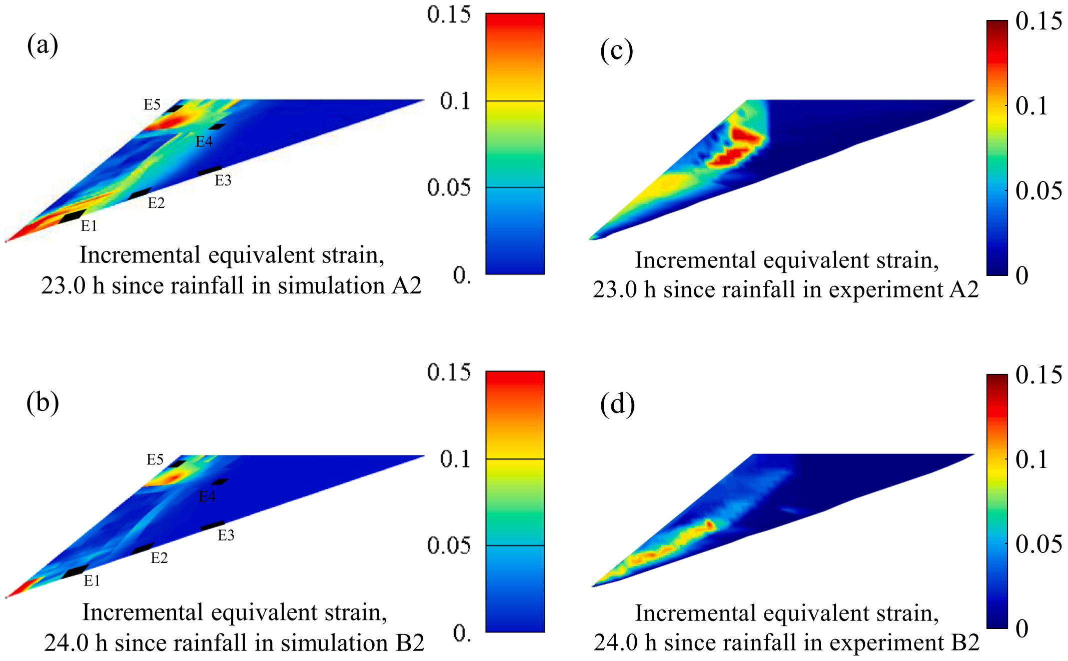

Incremental equivalent strain, 23.0 h since rainfall in simulation A2

Incremental equivalent strain, 23.0 h since rainfall in experiment A2

Incremental equivalent strain, 24.0 h since rainfall in simulation B2

Incremental equivalent strain, 24.0 h since rainfall in experiment B2

Fig. 16. Equivalent strains upon rainfall-induced landslides in simulations A2 (a) and B2 (b) and experiments A2 (c) and B2 (d).

concentrated deformation originating from the toe area and extending toward the upslope part. Additional work is required to describe how damage affected the soil strength so that the deformation of soil near the surface can be well reproduced. Eq. (19) used in the analysis could be regarded as a preliminary attempt; more sophisticated formulas needed to be worked out to achieve accurate initiation and development of soil deformation near the slope surface.

5.4. Soil displacement

The absolute displacement of three soil points (M1, M2, and M3 in Fig. 3) that moved downslope during post-shaking rainfall in simulations and experiments are provided in Fig. 17.

In Fig. 17(a), the simulated soil displacement has slightly earlier development of significant values starting about 20 h since the beginning of the rainfall, compared with the time of about 22 h in the experimental one. This is attributed to the permeability enhancement of soil near the slope shoulder. Also, as discussed previously, element E5

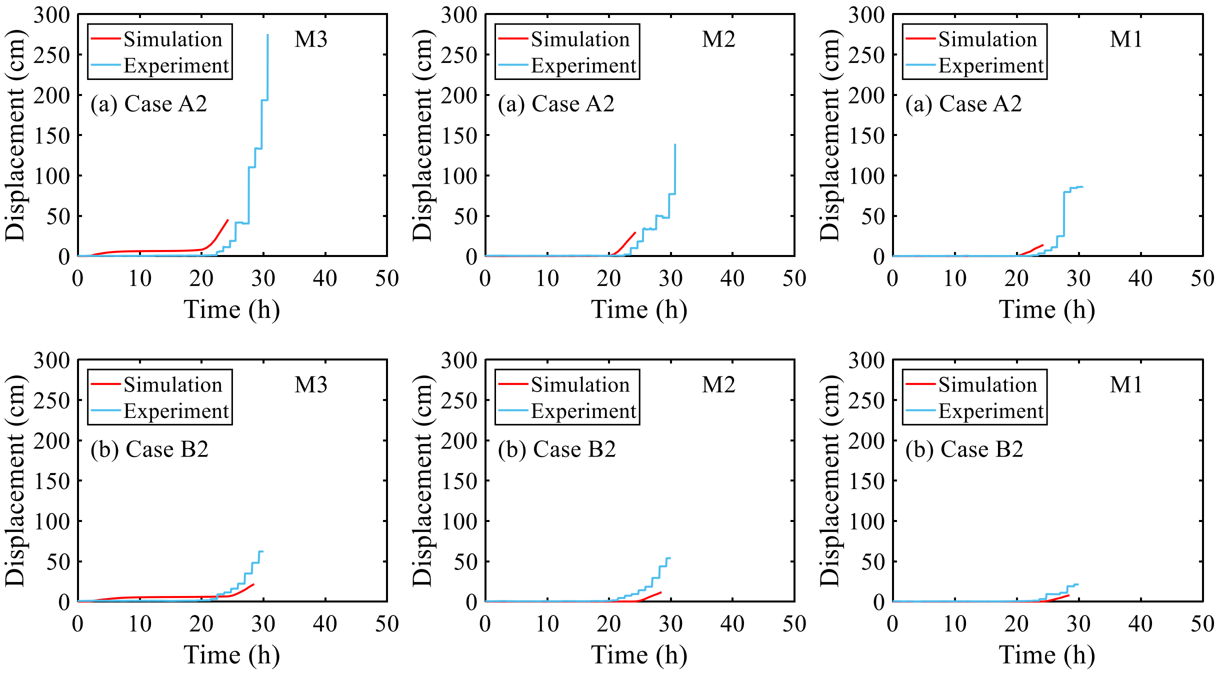

Fig. 17. Soil displacement in slopes during post-shaking rainfall in cases A2 and B2 (experimental data from Xu et al., 2022).

has already deformed at the initial stage, which was why the point M3 located in the one node of E5 had an earlier movement than M2 and M3. The simulated soil displacement during heavy rainfall basically reproduced the kinematics of the early stage of the slope failure as the soil movement and its velocity were consistent with the experimental results, but the whole landslide was not well reflected as the simulated displacement was still smaller than its experimental counterpart. In Fig. 17(b), the simulation has comparable evolution of soil displacement with the experiment for the slope under light rainfall. Due to a less severe failure process, the landslide kinematics upon failure was largely captured in the simulation despite slightly small values.

One noticeable feature about the soil displacement during heavy rainfall in case A2 is the large difference between simulation and experiment shown in Fig. 17(a); it is associated with several major factors including wetting-induced collapse, the deformation due to the change in stress ratio of soil, and post-failure landslide kinematics.

Rainfall infiltration usually leads to wetting-induced collapse, which is the volumetric compression caused by the reduction in suction at a given vertical stress (Alonso et al., 1990; Lawton et al., 1992). As the degree of saturation of soil increases during rainfall, the apparent unsaturated preconsolidation stress is decreased and the yield surface shrinks until it reaches the current position of the yield surface. Yielding is produced upon further wetting and as a result, the soil undergoes irrecoverable plastic strains and collapses. One drawback in the current constitutive model is the exclusion of wetting-induced shrinkage of the yield surface during rainfall, so the wetting-induced collapse was not reproduced in this study. The verification in the hydro-mechanical response of unsaturated soil to rainfall infiltration has not been completed; improvement on the applicability of this constitutive model is needed in the future study.

Regarding the yield function (see Appendix) in the present model, it uses the stress ratio between the deviatoric stress and effective stress to describe the yield surface, which is a cone in the principal stress space. When the mean effective stress decreases and the stress path moves toward the critical state line in Fig. 14, the large strain in Fig. 16 and displacement in Fig. 17 are generated as the soil shows elastoplastic behavior even when the yield surface does not consider the wetting-induced shrinkage. The soil deformation resulting from the change in stress ratio during rainfall was described adequately in the current analysis.

As the soil continues to deform until a certain large value like the maximum displacement of M3 in the simulation in Fig. 17(a), the iteration stops converging as the small deformation analysis is used in this study. For the further larger displacement in the experiment in Fig. 17 (a), it indicates the post-failure landslide displacement. At the post-failure stage of the landslide, the soil near the slope surface such as M3 has shown large displacement, which the current numerical model fails to simulate. This large deformation during the post-failure landslide could be quantitatively assessed by taking approaches such as the material point method (MPM) adopted by Liu et al. (2020) and Cuomo et al. (2021), while it was beyond the scope of this study.

However, under the rainfall with a lower intensity in case B2, the post-failure deformation is not significant compared to that in case A2, so the soil displacement in Fig. 17(b) is mainly dependent on the wetting-induced collapse and change in stress ratio during rainfall. Since the deformation due to collapse is not covered in the present analysis, the simulated displacement in Fig. 17(b) is basically smaller than the experimental displacement.

6. Conclusions

The response of slope subjected to post-shaking rainfall was studied in this paper. Coupled hydro-mechanical analyses were performed to evaluate the seepage and deformation of unsaturated slope employing the finite element (FE) numerical modeling technique, with the adoption of the proposed methods incorporating the effect of shaking on the permeability and strength of soil into the analyses.

The elastoplastic model and water retention model were calibrated using laboratory tests. The FE analysis of slope subjected to only rainfall and only earthquake was compared with the centrifuge experimental outcome and the simulation showed a good performance in reproducing slope response. Then, the effect of an earthquake on slope behavior during the following rainfall was investigated. Due to the seismic loading, a slip surface was generated within the slope and the shaking-induced deformation resulted in plastic shear modulus reduction and permeability change of soil along the slip surface. To include these two effects in the hydro-mechanical analysis of slope response to the following rainfall, this study considered the influence of shear strain dependent reduction in plastic shear modulus and adopted the Kozeny–Carman equation to connect the permeability and volumetric strain. In addition, the shaking-induced surface cracks, which were observed in the centrifuge experiments, were also considered in the numerical simulations by introducing the damage concept; the permeability enhancement and soil strength reduction were described mathematically. Afterward, the analyses of the response of slope to post-earthquake rainfall were carried out and results of pore water pressure, effective stress path, slope deformation, and soil displacement were evaluated.

Main conclusions were drawn as follows:

1. Once the earthquake caused a slip surface inside the slope, the effect of shaking should be incorporated in the hydro-mechanical analysis of slope response to the subsequent rainfall.
2. The shaking-induced reduction in plastic shear modulus of soil needed to be considered in the analysis of slope response to the following rainfall as it would affect the location of the slope failure and the severity of rainfall-induced landslide. The shaking-induced change in permeability of soil was considered using the Kozeny–Carman equation in the analysis, but results showed this effect was not significant enough to affect the slope deformation in this study. The shaking-induced surface cracks near the slope shoulder could be incorporated into the analysis by introducing the damage concept. The permeability enhancement and strength reduction were thus mathematically described and results showed that earthquake-induced damage greatly altered the slope failure characteristics.
3. The numerical analysis considering the above three effects based on the finite element method (FEM) showed a good performance in modeling the impact of shaking on the hydro-mechanical response of slope to the following rainfall. Stress paths were discussed to better understand the slope failure mechanism. Although the wetting-induced collapse and post-failure deformation were not considered, slope deformation and soil displacement during failure in simulations were generally consistent with the experimental results. However, the pore water pressure build-up during rainfall was not fully predicted especially under the heavy rainfall scenario.

The hydro-mechanical modeling framework in this study is useful to provide reference for the investigation into the failure mechanism of slope subjected to post-earthquake rainfall. Future work should be done to improve the description of shaking-induced cracks near the slope surface and consider wetting-induced collapse during rainfall infiltration.

CRediT authorship contribution statement

Jiawei Xu: Conceptualization, Methodology, Investigation, Software, Validation, Formal analysis, Visualization, Writing – original draft. **Kyohei Ueda:** Supervision, Writing – review & editing. **Ryosuke Uzuoka:** Supervision, Funding acquisition, Writing – review & editing, Software.

Declaration of Competing Interest

The authors declare that they have no known competing financial interests or personal relationships that could have appeared to influence the work reported in this paper.

Acknowledgment

This work was supported by JSPS KAKENHI Grant Number 21H04575.

Appendix

In the elastoplastic model, the extended von Mises yield function (Jiang and Kurath 1996; Golchin and Lashkari 2014) of the unsaturated soil is written as

$$f = \sqrt{3/2}\|\boldsymbol{r} - \boldsymbol{\eta}\| - k = 0 \tag{20}$$

where $\boldsymbol{r}$ is the stress ratio between deviatoric stress tensor s and mean effective stress $p^{'}$; k is a constant that defines the elastic region. The evolution of the back stress $\boldsymbol{\eta}$ is defined by the non-linear kinematic hardening model (Frederick and Armstrong, 2007; Dafalias et al., 2008), which is given by

$$\dot{\boldsymbol{\eta}} = a\left(\frac{2}{3}b\dot{\boldsymbol{e}}^{\mathrm{p}} - \boldsymbol{\eta}\dot{\varepsilon}_{\mathrm{d}}^{\mathrm{p}}\right) \tag{21}$$

where a and b are the material parameters related to the initial plastic shear modulus and stress ratio at failure; $\dot{\boldsymbol{e}}^{\mathrm{p}}$ is the plastic equivalent (deviatoric) strain rate tensor; $\dot{\varepsilon}_{\mathrm{d}}^{\mathrm{p}}$ equals $\sqrt{2/3}\|\dot{\boldsymbol{e}}^{\mathrm{p}}\|$.

To include the dependence of the plastic shear modulus on shear strain, the following equation is introduced to adjust the change in parameter a according to the magnitude of equivalent strain $\varepsilon_{\mathrm{d}}^{\mathrm{p}}$.

$$a = a_0 - \frac{a_0 - a_{\min}}{1 + (a_0 - a_{\min})\exp(-C_{\mathrm{ref}}\varepsilon_{\mathrm{d}}^{\mathrm{p}})} \tag{22}$$

where a_0, $a_{\min}$, and C_{ref} are the parameters that reproduce the cyclic tests on soil sample through element simulations; a_0 is related to the initial plastic shear modulus while $a_{\min}$ is related to the ultimate plastic shear modulus; C_{ref} controls the reduction of plastic shear modulus in a loading cycle. The larger C_{ref} is, the faster the plastic shear modulus will decrease. When C_{ref} is set as 0, the degradation of plastic shear modulus is neglected.

The plastic potential function g has a Cam-clay-type formula (Oka et al., 1999) written as

$$g = \sqrt{3/2}\|\boldsymbol{r} - \boldsymbol{\eta}\| + M_{\mathrm{m}}\ln\left(p^{'}/p_0^{'}\right) \tag{23}$$

where M_{m} is the critical state ratio; $p_0^{'}$ is the value of $p^{'}$ when $\|\boldsymbol{r} - \boldsymbol{\eta}\| = 0$.

The non-associated flow rule (Naghdi and Trapp, 1975; Oka et al., 1999) is adopted and the expressions of plastic deviatoric and volumetric strains are written as

$$\dot{\boldsymbol{\varepsilon}}^{\mathrm{p}} = \lambda \frac{\partial g}{\partial \boldsymbol{\sigma}} \tag{24}$$

$$\lambda = \lambda_1 \delta_{\mathrm{ij}} \delta_{\mathrm{kl}} + \lambda_2 \left(\delta_{\mathrm{ik}} \delta_{\mathrm{jl}} + \delta_{\mathrm{il}} \delta_{\mathrm{jk}} \right) \tag{25}$$

Namely,

$$\dot{\varepsilon}_{\mathrm{d}}^{\mathrm{p}} = 2\lambda_2 \frac{\partial g}{\partial q} \tag{26}$$

$$\dot{\varepsilon}_{\mathrm{v}}^{\mathrm{p}} = (3\lambda_1 + 2\lambda_2) \frac{\partial g}{\partial p'} \tag{27}$$

$$d = \frac{3\lambda_1 + 2\lambda_2}{2\lambda_2} \tag{28}$$

where λ is the plastic multiplier; λ_1 and λ_2 are generally dependent on the state parameters, e.g. stress and strain, and d is the coefficient of dilatancy controlling the ratio of the plastic volumetric strain increment to the plastic deviatoric strain increment.

The evolution rule of dilatancy d (Matsumaru and Uzuoka, 2016) is related to suction p^{c} and satisfies

$$d = \begin{cases} d_{\min} + (d_0 - d_{\min}) \exp\left(- p^{\mathrm{c}} / p_{\mathrm{ref}}^{\mathrm{c}} \right), p^{\mathrm{c}} > 0 \\ d_{\min}, p^{\mathrm{c}} \leq 0 \end{cases} \tag{29}$$

where d_0 and $d_{\min}$ are the initial and minimum dilatancy values; $p_{\mathrm{ref}}^{\mathrm{c}}$ is the reference suction used to control the dilatancy change.

The elastic relationship was described using another two parameters K^{e} and G^{e}

$$K^{\mathrm{e}} = K^* p'; \; G^{\mathrm{e}} = G^* p' \tag{30}$$

where K^{e} and G^{e} are the elastic bulk moduli and K^* and G^* are the dimensionless elastic moduli.

References

Alonso, E.E., Gens, A., Josa, A., 1990. A constitutive model for partially saturated soils. Geotechnique 40 (3), 405–430. https://doi.org/10.1680/geot.1990.40.3.405.

Bhattacherjee, D., Viswanadham, B.V.S., 2019. Centrifuge model studies on performance of hybrid geosynthetic-reinforced slopes with poorly draining soil subjected to rainfall. J. Geotech. Geoenviron. Eng. 145 (12), 1–13. https://doi.org/10.1520/GTJ20160254.

Biot, M.A., 1941. General theory of three-dimensional consolidation. J. Appl. Phys. 12 (2), 155–164.

Biot, M.A., 1962. Mechanics of deformation and acoustic propagation in porous media. J. Appl. Phys. 33 (4), 1482–1498.

Borja, R.I., White, J.A., 2010. Continuum deformation and stability analyses of a steep hillside slope under rainfall infiltration. Acta Geotech. 5 (1), 1–14. https://doi.org/10.1007/s11440-009-0108-1.

Cai, F., Ugai, K., 2004. Numerical analysis of rainfall effects on slope stability. Int. J. Geomech. 4 (2), 69–78. https://doi.org/10.1061/(ASCE)1532-3641(2004)4:2(69).

Carman, P.C., 1937. Fluid flow through granular beds. Trans. Instn. Chem. Engrs. 15, 150–166.

Chen, T., Sedigh, M., Jivkov, A.P., Seetharam, S.C., 2021a. A model for hydraulic conductivity of compacted bentonite–inclusion of microstructure effects under confined wetting. Geotechnique 71 (12), 1071–1084. https://doi.org/10.1680/jgeot.19.P.088.

Chen, X., Zhang, L., Zhang, L., Zhou, Y., Ye, G., Guo, N., 2021b. Modelling rainfall-induced landslides from initiation of instability to post-failure. Comput. Geotech. 129, 103877 https://doi.org/10.1016/j.compgeo.2020.103877.

Cheuk, C.Y., Ng, C.W.W., Sun, H.W., 2005. Numerical experiments of soil nails in loose fill slopes subjected to rainfall infiltration effects. Comput. Geotech. 32 (4), 290–303. https://doi.org/10.1016/j.compgeo.2005.02.005.

Childs, E.C., 1969. An introduction of the physical basis of soil water phenomena. John Wiley & Sons Ltd, London.

Cuomo, S., Perna, A.D., Martinelli, M., 2021. Modelling the spatio-temporal evolution of a rainfall-induced retrogressive landslide in an unsaturated slope. Eng. Geol. 294 (5), 106371 https://doi.org/10.1016/j.enggeo.2021.106371.

Dafalias, Y.F., Kourousis, K.I., Saridis, G.I., 2008. Multiplicative AF kinematic hardening in plasticity. Int. J. Solids. 45 (10), 2861–2880. https://doi.org/10.1016/j.ijsolstr.2008.01.001.

de Boer, R., 2000. Contemporary progress in porous media theory. Appl. Mech. Rev. 53 (12), 323–369. https://doi.org/10.1115/1.3097333.

Ehlers, W., Graf, T., Ammann, M., 2004. Deformation and localization analysis of partially saturated soil. Comput. Methods Appl. Mech. Eng. 193 (27–29), 2885–2910. https://doi.org/10.1016/j.cma.2003.09.026.

Frederick, C.O., Armstrong, P.J., 2007. A mathematical representation of the multiaxial Bauschinger effect. Mater. High Temp. 24 (1), 1–26. https://doi.org/10.1179/096034007X207589.

Froude, M.J., Petley, D.N., 2018. Global fatal landslide occurrence from 2004 to 2016. Nat. Hazards Earth Syst. Sci. 18 (8), 2161–2181. https://doi.org/10.5194/nhess-18-2161-2018.

Gallipoli, D., Wheeler, S.J., Karstunen, M., 2003. Modelling the variation of degree of saturation in a deformable unsaturated soil. Geotechnique 53 (1), 105–112. https://doi.org/10.1680/geot.2003.53.1.105.

Gao, Q.F., Zeng, L., Shi, Z.N., 2021. Effects of desiccation cracks and vegetation on the shallow stability of a red clay cut slope under rainfall infiltration. Comput. Geotech. 140, 104436 https://doi.org/10.1016/j.compgeo.2021.104436.

Ghorbani, J., Nazem, M., Carter, J.P., 2020. Dynamic compaction of clays: numerical study based on the mechanics of unsaturated soils. Int. J. Geomech. 20 (10), 04020195. https://doi.org/10.1061/(ASCE)GM.1943-5622.0001840.

Ghorbani, J., Airey, D.W., Carter, J.P., Nazem, M., 2021. Unsaturated soil dynamics: Finite element solution including stress-induced anisotropy. Comput. Geotech. 133, 104062 https://doi.org/10.1016/j.compgeo.2021.104062.

Golchin, A., Lashkari, A., 2014. A critical state sand model with elastic–plastic coupling. Int. J. Solids. 51 (15–16), 2807–2825. https://doi.org/10.1016/j.ijsolstr.2014.03.032.

Hu, R., Chen, Y., Zhou, C., 2011. Modeling of coupled deformation, water flow and gas transport in soil slopes subjected to rain infiltration. Sci. China Technol. Sci. 54 (10), 2561–2575. https://doi.org/10.1007/s11431-011-4504-z.

Hu, R., Chen, Y.F., Liu, H.H., Zhou, C.B., 2013. A water retention curve and unsaturated hydraulic conductivity model for deformable soils: consideration of the change in pore-size distribution. Geotechnique 63 (16), 1389–1405. https://doi.org/10.1680/geot.12.P.182.

Hu, R., Chen, Y.F., Liu, H.H., Zhou, C.B., 2016. A coupled two-phase fluid flow and elastoplastic deformation model for unsaturated soils: theory, implementation, and application. Int. J. Numer. Anal. Meth. Geomech. 40, 1023–1058. https://doi.org/10.1002/nag.2473.

Huang, R., Pei, X., Fan, X., Zhang, W., Li, S., Li, B., 2012. The characteristics and failure mechanism of the largest landslide triggered by the Wenchuan earthquake, May 12, 2008. China. Landslides 9 (1), 131–142. https://doi.org/10.1007/s10346-011-0276-6.

Jiang, Y., Kurath, P., 1996. Characteristics of the Armstrong-Frederick type plasticity models. Int. J. Plast. 12 (3), 387–415. https://doi.org/10.1016/S0749-6419(96)00013-7.

Khalili, N., Habte, M., Zargarbashi, S., 2008. A fully coupled flow deformation model for cyclic analysis of unsaturated soils including hydraulic and mechanical hystereses. Comput. Geotech. 35 (6), 872–889. https://doi.org/10.1016/j.compgeo.2008.08.003.

Khattak, G.A., Owen, L.A., Kamp, U., Harp, E.E., 2010. Evolution of earthquake-triggered landslides in the Kashmir Himalaya, northern Pakistan. Geomorphology 115 (1–2), 102–108. https://doi.org/10.1016/j.geomorph.2009.09.035.

Khoei, A., Mohammadnejad, T., 2011. Numerical modeling of multiphase fluid flow in deforming porous media: a comparison between two- and three-phase models for seismic analysis of earth and rockfill dams. Comput. Geotech. 38 (2), 142–166. https://doi.org/10.1016/j.compgeo.2010.10.010.

Kobayashi, Y., 1971. Effects of earthquakes on ground (I): ground cracking, soil liquefaction, and sliding of slopes. J. Phys. Earth 19 (3), 217–229. https://doi.org/10.4294/jpe1952.19.217.

Konrad, J.M., Ayad, R., 1997. An idealized framework for the analysis of cohesive soils undergoing desiccation. Can. Geotech. J. 34 (4), 477–488. https://doi.org/10.1139/t97-015.

Kozeny, J., 1927. Uber kapillare leitung der wasser in boden. Stizungsber Akad Wiss Wien 136 (2a), 271–306 in German.

Kramer, S.L., 1996. Geotechnical earthquake engineering. Prentice-Hall, New Jersey.

Laloui, L., Ferrari, A., Li, C., Eichenberger, J., 2016. Hydro-mechanical analysis of volcanic ash slopes during rainfall. Geotechnique 66 (3), 220–231. https://doi.org/10.1680/jgeot.15.LM.001.

Lawton, E.C., Fragaszy, R.J., Hetherington, M.D., 1992. Review of wetting-induced collapse in compacted soil. J. Geotech. Eng. 118 (9), 1376–1394.

Levatti, H.U., Prat, P.C., Ledesma, A., 2019. Numerical and experimental study of initiation and propagation of desiccation cracks in clayey soils. Comput. Geotech. 105, 155–167. https://doi.org/10.1016/j.compgeo.2018.09.015.

Lewis, R.W., Schrefler, B.A.S., 1998. The Finite Element Method in the Static and Dynamic Deformation and Consolidation of Porous Media, second ed. Wiley, London.

Li, J.H., Zhang, L.M., 2010. Geometric parameters and REV of a crack network in soil. Comput. Geotech. 37 (4), 466–475. https://doi.org/10.1016/j.compgeo.2010.01.006.

Li, J.H., Zhang, L.M., Li, X., 2011. Soil-water characteristic curve and permeability function for unsaturated cracked soil. Can. Geotech. J. 48 (7), 1010–1031. https://doi.org/10.1139/t11-027.

Lin, C.W., Shieh, C.L., Yuan, B.D., Shieh, Y.C., Liu, S.H., Lee, S.Y., 2004. Impact of Chi-Chi earthquake on the occurrence of landslides and debris flows: example from the Chenyulan River watershed, Nantou. Taiwan. Eng. Geol. 71 (1–2), 49–61. https://doi.org/10.1016/S0013-7952(03)00125-X.

Liu, R., Han, Y., Xiao, J., Wang, T., 2020a. Failure mechanism of TRSS mode in landslides induced by earthquake. Sci. Rep. 10, 21326. https://doi.org/10.1038/s41598-020-78503-y.

Liu, X., Wang, Y., Li, D.Q., 2020b. Numerical simulation of the 1995 rainfall-induced Fei Tsui Road landslide in Hong Kong: new insights from hydro-mechanically coupled material point method. Landslides 17 (12), 2755–2775. https://doi.org/10.1007/s10346-020-01442-2.

Lu, N., Likos, W.J., 2004. Unsaturated soil mechanics. Wiley, Hoboken.

Lu, Y.L., Elsworth, D., Wang, L.G., 2013. Microcrack-based coupled damage and flow modeling of fracturing evolution in permeable brittle rocks. Comput. Geotech. 49, 226–244. https://doi.org/10.1016/j.compgeo.2012.11.009.

Maleki, K., Pouya, A., 2010. Numerical simulation of damage–permeability relationship in brittle geomaterials. Comput. Geotech. 37 (5), 619–628. https://doi.org/10.1016/j.compgeo.2010.03.009.

Matsumaru, T., Uzuoka, R., 2016. Three-phase seepage-deformation coupled analysis about unsaturated embankment damaged by earthquake. Int. J. Geomech. 16 (5), C4016006. https://doi.org/10.1061/(ASCE)GM.1943-5622.0000699.

Mori, T., Uzuoka, R., Chiba, T., Kamiya, K., Kazama, M., 2011. Numerical prediction of seepage and seismic behaviour of unsaturated fill slope. Soils Found. 51 (6), 1075–1090. https://doi.org/10.3208/sandf.51.1075.

Morris, P.H., Graham, J., Williams, D.J., 1992. Cracking in drying soils. Can. Geotech. J. 29 (2), 263–277. https://doi.org/10.1139/t92-030.

Moriwaki, H., Inokuchi, T., Hattanji, T., Sassa, K., Ochiai, H., Wang, G., 2004. Failure processes in a full-scale landslide experiment using a rainfall simulator. Landslides 1 (4), 277–288. https://doi.org/10.1007/s10346-004-0034-0.

Muraleetharan, K.K., Liu, C., Wei, C., Kibbey, T.C.G., Chen, L., 2009. An elastoplatic framework for coupling hydraulic and mechanical behavior of unsaturated soils. Int. J. Plast. 25 (3), 473–490. https://doi.org/10.1016/j.ijplas.2008.04.001.

Naghdi, P.M., Trapp, J.A., 1975. Restrictions on constitutive equations of finitely deformed elastic-plastic materials. Q. J. Mech. Appl. Math. 28 (1), 25–46. https://doi.org/10.1093/qjmam/28.1.25.

Ni, J.J., Leung, A.K., Ng, C.W.W., Shao, W., 2018. Modelling hydro-mechanical reinforcements of plants to slope stability. Comput. Geotech. 95, 99–109. https://doi.org/10.1016/j.compgeo.2017.09.001.

Ng, C.W.W., Kamchoom, V., Leung, A.K., 2016. Centrifuge modelling of the effects of root geometry on transpiration-induced suction and stability of vegetated slopes. Landslides 13 (5), 925–1938. https://doi.org/10.1007/s10346-015-0645-7.

Noda, T., Yoshikawa, T., 2015. Soil–water–air coupled finite deformation analysis based on a rate-type equation of motion incorporating the SYS Cam-clay model. Soils Found. 55 (1), 45–62. https://doi.org/10.1016/j.sandf.2014.12.004.

Oh, S., Lu, N., 2015. Slope stability analysis under unsaturated conditions: case studies of rainfall-induced failure of cut slopes. Eng. Geol. 184 (14), 96–103. https://doi.org/10.1016/j.enggeo.2014.11.007.

Oka, F., Yashima, A., Tateishi, A., Taguchi, T., Yamashita, S., 1999. A cyclic elasto-plastic constitutive model for sand considering a plastic-strain dependence of the shear modulus. Geotechnique 49 (5), 661–680. https://doi.org/10.1680/geot.1999.49.5.661.

Olivella, S., Alonso, E.F., 2008. Gas flow through clay barriers. Geotechnique 58 (3), 157–176. https://doi.org/10.1680/geot.2008.58.3.157.

Oka, F., Tsai, P., Kimoto, S., Kato, R., 2012. Damage patterns of river embankments due to the 2011 off the Pacific Coast of Tohoku Earthquake and a numerical modeling of the deformation of river embankments with a clayey subsoil layer. Soils Found. 52 (5), 890–909. https://doi.org/10.1016/j.sandf.2012.11.010.

Peron, H., Hueckel, T., Laloui, L., Hu, B., 2009. Fundamentals of desiccation cracking of fine-grained soils: experimental characterisation and mechanisms identification. Can. Geotech. J. 46 (10), 1177–1201. https://doi.org/10.1139/T09-054.

Petley, D., 2012. Global patterns of loss of life from landslides. Geology 40 (10), 927–930. https://doi.org/10.1130/G33217.1.

Pogacnik, J., O'Sullivan, M., O'Sullivan, J., 2014. A damage mechanics approach to modeling permeability enhancement in thermo-hydro-mechanical simulations, in: Proceedings of the 39th Workshop on Geothermal Reservoir Engineering, Stanford University, Stanford, pp. 369–380.

Qi, S., Vanapalli, S.K., 2015. Hydro-mechanical coupling effect on surficial layer stability of unsaturated expansive soil slopes. Comput. Geotech. 70, 68–82. https://doi.org/10.1016/j.compgeo.2015.07.006.

Ravichandran, N., Muraleetharan, K.K., 2009. Dynamics of unsaturated soils using various finite element formulations. Int. J. Numer. Anal. Methods Geomech. 33, 611–631. https://doi.org/10.1002/nag.737.

Stahl, T., Bilderback, E.L., Quigley, M.C., Nobes, D.C., Massey, C.I., 2014. Coseismic landsliding during the Mw 7.1 Darfield (Canterbury) earthquake: implications for paleoseismic studies of landslides. Geomorphology 24, 114–127. https://doi.org/10.1016/j.geomorph.2014.03.020.

Schrefler, B.A., 2002. Mechanics and thermodynamics of saturated/unsaturated porous materials and quantitative solutions. Appl. Mech. Rev. 55 (4), 351–388. https://doi.org/10.1115/1.1484107.

Sitarenios, P., Casini, F., Askarinejad, A., Springman, S., 2021. Hydro-mechanical analysis of a surficial landslide triggered by artificial rainfall: the Ruedlingen field experiment. Geotechnique 71 (2), 96–109. https://doi.org/10.1680/jgeot.18.P.188.

Switala, B.M., Wu, W., 2018. Numerical modelling of rainfall-induced instability of vegetated slopes. Geotechnique 68 (6), 481–491. https://doi.org/10.1680/jgeot.16.P.176.

Take, W.A., Bolton, M.D., Wong, P.C.P., Yeung, F.J., 2004. Evaluation of landslide triggering mechanisms in model fill slopes. Landslides 1 (3), 173–184. https://doi.org/10.1007/s10346-004-0025-1.

Tang, Y., Wu, W., Yin, K., Wang, S., Lei, G., 2019. A hydro-mechanical coupled analysis of rainfall induced landslide using a hypoplastic constitutive model. Comput. Geotech. 112, 284–292.

Tang, C., Zhu, J., Qi, X., Ding, J., 2011. Landslides induced by the Wenchuan earthquake and the subsequent strong rainfall event: a case study in the Beichuan area of China. Eng. Geol. 122 (1–2), 22–33. https://doi.org/10.1016/j.enggeo.2011.03.013.

Tarantino, A., 2009. A water retention model for deformable soils. Geotechnique 59 (9), 751–762. https://doi.org/10.1680/geot.7.00118.

Towhata, I., 2008. Geotechnical earthquake engineering. Springer, Berlin, Heidelberg. https://doi.org/10.1007/978-3-540-35783-4.

Usui, Y., Shimada, H., Innami, H., Amao, K., Higashi, K., Kawabata, H., 2013. Case study on heavy rainfall-induced reactivation of seismically disturbed slope caused by the 2011 off the Pacific Coast of Tohoku Earthquake, in: Ugai, K., Yagi, H., Wakai, A. (Eds), Earthquake-Induced Landslides. Springer, Berlin, Heidelberg, pp. 323–329. https://doi.org/10.1007/978-3-642-32238-9_33.

Upreti, K., Leong, E.C., 2021. Effect of mean grain size on shear modulus degradation and damping ratio curves of sands. Geotechnique 71 (3), 205–215. https://doi.org/10.1680/jgeot.18.P.169.

Utili, S., 2013. Investigation on the stability of slopes with cracks by limit analysis. Geotechnique 63 (2), 140–154. https://doi.org/10.1680/geot.11.P.068.

Uzuoka, R., Borja, R.I., 2012. Dynamics of unsaturated poroelastic solids at finite strain. Int. J. Numer. Anal. Meth. Geomech. 36, 1535–1573. https://doi.org/10.1002/nag.1061.

Uzuoka, R., Kurihara, T., Kazama, M., Seno, N., 2008. Finite element analysis of coupled system of unsaturated soil and water using aerial elements. Proc. Conf. Comput. Eng. Sci. 13, 219–222.

van Genuchten, M.T., 1980. A closed-form equation for predicting the hydraulic conductivity of unsaturated soils. Soil Sci. Soc. Am. J. 44, 892–898. https://doi.org/10.2136/sssaj1980.03615995004400050002x.

Vucetic, M., Dubry, R., 1991. Effect of soil plasticity on cyclic response. J. Geotech. Eng. 117 (1), 89–107. https://doi.org/10.1061/(ASCE)0733-9410(1991)117:1(89).

Wang, L., Hu, W., Sun, D., Li, L., 2019. 3D stability of unsaturated soil slopes with tension cracks under steady infiltrations. Int. J. Numer. Anal. Methods Geomech. 43 (6), 1184–1206. https://doi.org/10.1002/nag.2889.

Wang, S., Idinger, G., Wu, W., 2021. Centrifuge modelling of rainfall-induced slope failure in variably saturated soil. Acta Geotech. 16 (9), 2899–2916. https://doi.org/10.1007/s11440-021-01169-x.

Wang, G., Sassa, K., 2001. Factors affecting rainfall-induced fowslides in laboratory flume tests. Geotechnique 51 (7), 587–599. https://doi.org/10.1680/geot.2001.51.7.587.

Wang, Z.F., Li, J.H., Zhang, L.M., 2011. Influence of cracks on the stability of a cracked soil slope, in: Jotisankasa et al. (Eds.), Unsaturated Soils: Theory and Practice. Thailand, pp. 721–727.

Wang, X., Yu, P., Yu, J., Yu, Y., 2018. Simulated crack and slip plane propagation in soil slopes with embedded discontinuities using XFEM. Int. J. Geomech. 18 (2), 1–17. https://doi.org/10.1061/(ASCE)GM.1943-5622.0001290, 04018170.

Xiong, Y., Bao, X., Ye, B., Zhang, F., 2014. Soil–water–air fully coupling finite element analysis of slope failures in unsaturated ground. Soils Found. 54 (3), 377–395. https://doi.org/10.1016/j.sandf.2014.04.007.

Xu, J., Ueda, K., Uzuoka, R., 2022. Evaluation of failure of slopes with shaking-induced cracks in response to rainfall. Landslides 19 (1), 119–136. https://doi.org/10.1007/s10346-021-01734-1.

Yang, K.H., Uzuoka, R., Thuo, J.N., Lin, G.L., Nakai, Y., 2017. Coupled hydro-mechanical analysis of two unstable unsaturated slopes subject to rainfall infiltration. Eng. Geol. 21 (12), 13–30. https://doi.org/10.1016/j.enggeo.2016.11.006.

Yang, K.H., Thuo, J.N., Huynh, V.D.A., Nguyen, T.S., Portelinha, F.H.M., 2018. Numerical evaluation of reinforced slopes with various backfill-reinforcement-drainage systems subject to rainfall infiltration. Comput. Geotech. 96, 25–39. https://doi.org/10.1016/j.compgeo.2017.10.012.

Yerro, A., Alonso, E.E., Pinyol, N.M., 2015. The material point method for unsaturated soils. Geotechnique 65 (3), 201–217. https://doi.org/10.1680/geot.14.P.163.

Yoshikawa, T., Noda, T., Kodaka, T., Takaine, T., 2016. Analysis of the effect of groundwater level on the seismic behavior of an unsaturated embankment on clayey ground. Soil Dyn. Earthq. Eng. 85, 217–230. https://doi.org/10.1016/j.soildyn.2016.02.008.

Zeng, L., Xiao, L.-Y., Zhang, J.-H., Gao, Q.-F., 2020. Effect of the characteristics of surface cracks on the transient saturated zones in colluvial soil slopes during rainfall. Bull. Eng. Geol. Environ. 79 (2), 699–709.

Zhang, B., Muraleetharan, K.K., 2019. Implementation of a hydromechanical elastoplastic constitutive model for fully coupled dynamic analysis of unsaturated soils and its validation using centrifuge test results. Acta Geotech. 14 (2), 347–360. https://doi.org/10.1007/s11440-018-0752-4.

Zhang, F., Xiong, Y., Zhang, S., Ye, B., 2014a. Thermo-hydro-mechanical-air coupling finite element method and its application to multi-phase problems. J. Rock Mech. Geotech. Eng. 6 (2), 77–98. https://doi.org/10.1016/j.jrmge.2014.01.010.

Zhang, Z., Fu, X., Sheng, Q., Du, Y., Zhou, Y., Huang, J., 2021. Stability of cracking deposit slope considering parameter deterioration subjected to rainfall. Int. J. Geomech. 21 (7) https://doi.org/10.1061/(ASCE)GM.1943-5622.0002045.

Zhang, Z.B., Zhou, H., Zhao, Q.G., Lin, H., Peng, X., 2014b. Characteristics of cracks in two paddy soils and their impacts on preferential flow. Geoderma 228–229, 114–121. https://doi.org/10.1016/j.geoderma.2013.07.026.

Zhang, J., Zhu, D., Zhang, S., 2020. Shallow slope stability evolution during rainwater infiltration considering soil cracking state. Comput. Geotech. 117, 103285 https://doi.org/10.1016/j.compgeo.2019.103285.